

Solar Radiation Anomaly Events Modeling Using Spatial-Temporal Mutually Interactive Processes

Minghe Zhang*, Chen Xu*, Andy Sun, Feng Qiu, Yao Xie

January 2021

Abstract

Modeling and predicting solar events, in particular, the solar ramping event is critical for improving situational awareness for solar power generation systems. Solar ramping events are significantly impacted by weather conditions such as temperature, humidity, and cloud density. Discovering the correlation between different locations and times is a highly challenging task since the system is complex and noisy. We propose a novel method to model and predict ramping events from spatial-temporal sequential solar radiation data based on a spatio-temporal interactive Bernoulli process. We demonstrate the good performance of our approach on real solar radiation datasets.

1 Introduction

Solar power installations are becoming common in residential and commercial areas, largely due to their decreasing costs. However, the power system is vulnerable to some anomalies such as rainstorm or hurricane, which cost greatly to restoration. As a result, detecting and predicting abnormal events from the spatial-temporal series plays a vital role in the solar system, aiming to capture the variety of intrinsic reasons for the anomalies. For example, the rainstorm and drought would bring out different types and patterns of anomalies. In many cases, the abnormal event will also start at one location and then propagate to its neighbors with a time delay, leading to spatial-temporal correlation among anomalies. Thus it is crucial to make observations at multiple locations, which correspondingly form the spatial-temporal series.

In this paper, we address non-stationarity and strong spatial-temporal correlation through the following contributions:

- **Strong spatial-temporal correlation:** We present a spatial-temporal Bernoulli process (also extended to categorical observations), which is proposed by [19]. The model can flexibly capture the spatial-temporal correlations and interactions without assuming time-decaying influence. It can also efficiently make predictions for any location at any future time for timely ramp event detection.
- **Non-stationarity:** First, we map the raw continuous solar observations into discrete binary or categorical events by comparing the current radiation level with a sliding window. The sliding window captures the moving average of the sequence, which accounts for the non-stationarity in the process. Each of the extracted discrete events is also known as ramping event [12, 8, 20] which is defined to be an abrupt slope increase or decrease in a time series and is widely used in power system such as wind and solar. Second, to address non-stationarity when making online decisions of a future ramping event, we formulate dynamic decision thresholds and compare the prediction results with those under static thresholds.

To demonstrate the flexibility and performance of the proposed model, we perform extensive real-data analysis using solar radiation data collected across different states in the US over several years.

The rest of the paper is then organized as follows: Section 2 presents the problem setup and aforementioned spatial-temporal models. More specifically, in Section 2.1, we address non-stationarity in raw sequential observations by transforming them into ramping events. In Section 2.2, we capture spatial-temporal

*first two authors made equal contributions.

correlations between these abnormal events with the single-state and the multi-state model, respectively. Section 3 presents estimations of parameters via the Least Square method and the Maximum Likelihood method, with theoretical analyses on the quality of estimates. We also describe prediction approaches by utilizing static or dynamic thresholds in this section. Section 4 presents comprehensive experiment results to show the computational efficiency and accuracy of our method. Finally, in Section 5, we summarize the contributions, limitations, and possible extensions in this paper.

1.1 Literature

A lot of previous works on solar radiation modeling [27] focus on predicting the average daily and hourly global radiation, beam radiation, and diffuse radiation. Other solar researches by [5] target at utilizing solar radiation to study the climate. Furthermore, most of the works explore the properties of solar radiation in some specific locations [24, 9, 13]. While these works are important for better modeling solar power, our present work focuses on a different task—ramping event modeling.

Many works directly model wind and solar ramping event data. A line of work started by [11] directly uses historical data without modeling by adopting the Swinging Door Algorithm (SDA) commonly used in data compression. Later, [6], and [7] refines the SDA, proposes an optimized SDA using dynamic programming, and demonstrates its use on various wind and solar ramping event modeling tasks. However, these works do not have theoretical guarantees on the accuracy of detected ramping events nor intentionally consider spatial-temporal correlations. Among recent works, [1] uses ensemble-based probabilistic forecasts and post-process the forecasts through adjustments. Being well-established, the forecasting procedures, however, need access to many features besides the radiation levels, so its applicability can be hampered by limited data. To address the problem with limited data, [31] proposes a forewarning method using credal network and Dirichlet model to study power change caused by meteorological fluctuation. However, this work mainly studies the effect of an exogenous variable (meteorological fluctuation) on the changes in solar radiations, and the authors did not propose how to convert their probabilistic forecast into reliable multivariate classification. Another work by [4] tackles uncertainty quantification of ramping event forecast through providing data-driven probability upper bounds. However, they do not address spatial correlations, and it is known that distributionally-robust estimations can sometimes be too conservative. As a result, dynamic solar ramping event modeling still remains a great challenge, especially under strong spatial-temporal correlation.

Meanwhile, there has been much advance on stochastic event modeling outside the energy research community, which takes temporal correlation into account. These works date back to Hawkes process model [16] and self-correcting point process model [18]. More recently, many are inspired by these works to provide statistical methods for modeling temporal point processes. [26] proposes a multivariate point process regression model to analyze neuronal spike trains. [28] models event propagation using graph biased temporal point process to leverage structural information from the graph. An earlier application by [22] models rumors prevalence on social media via a log-Gaussian Cov process to learn the underlying temporal probabilistic model. On the other hand, methods using deep learning techniques have also been widely considered. For example, RNN or LSTM cells are used in [10, 23] to memorize the influence of historical events. A recent work [30] uses attention to model the historical information in the point process. There is also work that uses imitation learning algorithm [21] to learn a generator that captures the same time dependency pattern. While being diverse and useful, none of these works try to consider spatial influence, mainly due to the structural differences between time and space and the computational difficulties in higher dimensions. Recent work by [29] uses tail-up models for spatial modeling and attention mechanism to capture the time dependency for traffic flows. Still, the lack of theoretical guarantee and differences in modeling purpose makes it hard to be applied here.

Research work on anomaly detection (a.k.a. outlier detection) in the time series analysis area has also been active for decades, which could be traced back to [14]’s work in the 1960s. There are a significant number of conventional works on the topic, such as [2, 3, 15]. Also, many works use a modern deep learning framework to deal with more complex patterns such as [17] and more. However, none of these works have a flexible anomaly detection model under strong spatial-temporal correlation for non-stationary data.

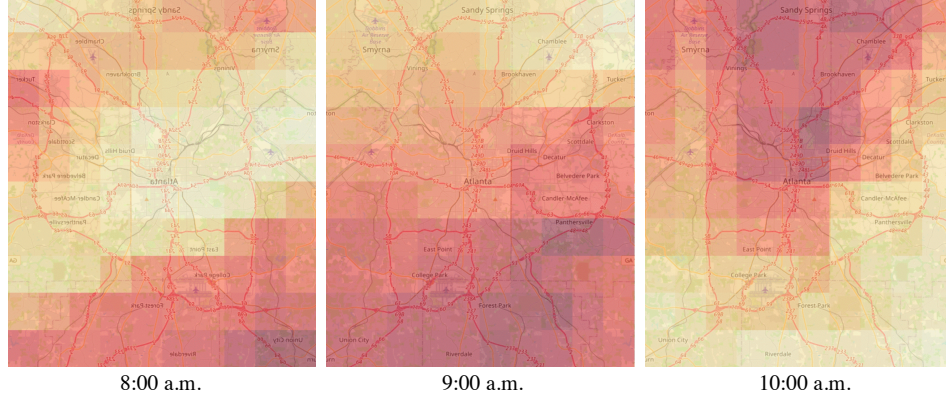


Figure 1: Illustration on spatial-temporal dynamic of solar activities at different locations (around Atlanta area). The darker color in the map represents less solar radiation. At 8:00 a.m., South Atlanta has less solar radiation than the average, while two hours later, it is clear that the low-radiation area has moved northward. This shows that there could be an abnormal event starting from the south but moving to the north.

2 Problem Setup

Given a spatial-temporal sequence data $\{x_{t'k} \in \mathbb{R} : t' = 1, \dots, nT; k = 1, \dots, K\}$ where T denotes the time horizon (number of days), n denotes the number of observations each day per location and K denotes the total number of locations. Our goal is to model and predict the anomaly events efficiently and quickly. However, it is common to have imbalanced data in the solar power system, which means it is quite rare to have an anomaly. Thus taking the noisy raw observations directly for modeling and prediction tasks could be time-consuming and misleading. Such consideration leads us to first extract ramping events from the raw sequence. Ramping events are broadly used to represent abnormal events in a sequence of observations,

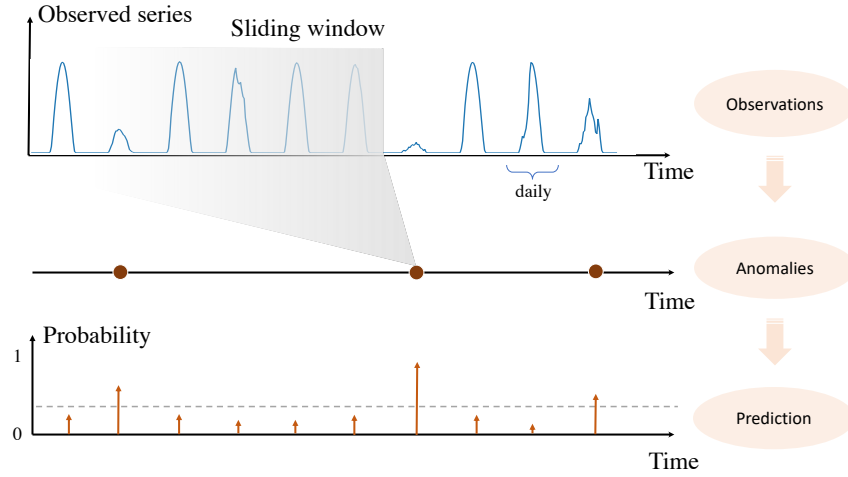


Figure 2: Illustration on the procedure for anomaly extraction and recovery using **real data** observations in Atlanta: first, the raw time series are fed into a sliding window sequentially. Given the set of historical events, we then calculate its $1 - \delta$ quantile; the current event is considered abnormal if it lies beyond or below the upper and lower δ quantile values. We then fit the extracted ramping events into our proposed model and recover the β parameters to make future anomaly predictions: we detect an anomaly if its probability lies above a certain threshold (the grey dotted line of the bottom figure). For non-stationary data, we might need dynamic thresholds rather than static ones, as shown in the figure.

and such events usually have a significant correlation over space and time. For instance, when a cloud floats over a field, it reduces the solar radiation and, therefore, the power generation at one particular location at that time. As the cloud moves, the nearby locations may be covered by the cloud in the next moment, and the power output becomes low in the neighborhoods. The direction of the cloud moving is random, as it depends on many complex factors. But we could say in a probabilistic sense that once a ramping event happens at one particular location, the chances will be higher for the nearby locations to experience the ramping events. Figure 1 gives an illustration to explain how abnormal events (low radiation areas are colored darker in this case) are spatially and temporally correlated. As a result, the probabilistic model that we introduce for solar ramping events in this paper could be a natural fit. It is reasonable to explore the correlations between locations in the model. Figure 2 illustrates the general procedure that began from real raw observations in Atlanta. We first converted them into abnormal events, then fit a statistical model to make further predictions.

A few challenges to tackle the problem of modeling and prediction for solar ramping events include (i) how to jointly capture the spatial and temporal correlations clearly; (ii) how to convert the probabilistic predictions into ramping event decisions; (iii) how to make real-time predictions of the solar ramping events based on the model, especially under non-stationary cases. We will discuss our solutions in the following subsections.

We list all the notations in Table 1 for quick reference. We remark that since ramping events are abnormal, we use abnormal events/anomaly and ramping events interchangeably.

Table 1: Table of Notations

$x_{t'k}$	\triangleq	Solar radiation observation at time t' (half-hourly) and location k
T	\triangleq	Time horizon (number of days)
n	\triangleq	Number of daily observations
K	\triangleq	Total number of locations
M	\triangleq	Total number of states for a ramping event
w_1	\triangleq	Sliding window length for extracting ramping events
w_2	\triangleq	Sliding window length for adjusting dynamic threshold in anomaly detection
d	\triangleq	Memory depth in mutually interactive process model
δ	\triangleq	Quantile for extracting ramping events
α	\triangleq	Adjusting factor for online threshold calculation in anomaly detection
ϵ	\triangleq	Tolerance when building confidence intervals for parameters and anomaly probabilities
ω_{tk}	\triangleq	$\begin{cases} \neq 0, & \text{if an anomaly happens at time } t \text{ (daily) and location } k \\ = 0, & \text{otherwise} \end{cases}$

2.1 From radiation data to ramping events

We first convert raw sequential observations into ramping events with single and multiple states, respectively.

Single-State: We first describe how we transform raw sequences $\{x_{t'k}\}$ described in the problem setup section into single-state ramping event sequences $\{\omega_{tk}\}$, where each $\omega_{tk} \in \{0, 1\}$ has only one non-zero state (denoted as 1) for a given time t and location k , indicating possible existence of an anomaly. The time indices of the two sequences have different physical meanings because the transformation of $\{x_{t'k}\}$ (e.g., calculating empirical confidence intervals of subsequences) alters how many data points are available at each location k . In this paper, we group the raw radiation observations in a single day at a location k into a set of data points if we have n sequential radiation observations recorded every day at different times, which

means while $t' \in [1, nT]$, we have $t \in [1, T]$. We will further see that we could extract accurate anomalies from the raw data by comparing every data point in the set with corresponding histories.

After this transformation, we perform extraction of ramping event sequences $\{\omega_{tk}\}$ from $\{x_{t'k}\}$. Noting that we have n observations $\{x_{t'k}\}$ where $t' = 1, 2, \dots, n$ at k -th location and t -th day, we choose a sliding window of size w_1 , which contains the past w_1 days of sub-sequential observations. We denote the past w_1 -days' history as

$$\mathbf{x}_{t-w_1, k}^{t-1} := \{x_{t'k} : t' = (t - w_1)n, (t - w_1)n + 1, \dots, nt - 1\}.$$

Then, we sort these values and compare every half-hourly observation in $\{x_{t'k}\}$ with the δ and $1 - \delta$ quantile values, where δ is a pre-defined threshold to control the density of ramping events. We define $\omega_{tk} = 1$ if $\alpha\%$ of $\{x_{t'k}\}$ in day t is either above the $1 - \delta$ quantile value or below the δ quantile value. We perform the extraction at all locations to get $\{\omega_{tk}\}$.

Multi-State: We note that single-state ramping events do not show the type to which the ramping event belongs (i.e., a ramping event may have either too high or too low post-smoothing radiation level). To show the type, we extract $\{\omega_{tk}\}$ using the same approach from $\{x_{t'k}\}$, but allows $\omega_{tk} \in \{0, 1, \dots, M\}$. Each non-zero state denotes a different type, such as high, low, extremely high, etc. We model both single-state and two-state ramping events for the experiments, where the two non-zero states show the current radiation level is too high (encoded as 1) or too low (encoded as 2). We define the two-state ramping events with the same sliding window technique, so that ω_{ts} is 1 if more than $\alpha\%$ of $\{x_{t'k}\}$ in day t is above the $1 - \delta$ quantile value, 2 if more than $\alpha\%$ of $\{x_{t'k}\}$ in day t is below the δ quantile value, and 0 otherwise.

2.2 Spatial-temporal generalized Bernoulli model

In this section, we fit a generalized Bernoulli model on extracted spatial-temporal ramping events.

Single-state model: We first define notations to be used in the single-state model. Given discrete time $t, t \in \{1, \dots, T\}$ and space indices $k, k \in \{1, \dots, K\}$, Our observed data is denoted as a data matrix of observations at all locations:

$$\boldsymbol{\omega}^T = \{\omega_{tk}, 1 \leq t \leq T, 1 \leq k \leq K\},$$

where $\omega_{tk} \in \{0, 1\}$, and given a memory depth d ,

$$\boldsymbol{\omega}_{t-d}^t = \{\omega_{sk}, t - d \leq s \leq t, 1 \leq k \leq K\}.$$

In other words, $\boldsymbol{\omega}_{t-d}^t$ is a data matrix that contains a set of observations at all locations from time $t - d$ up to time t .

We aim to build a parametric probabilistic model for these sequences of anomalies. Specifically, we assume that for $t \geq 1$, the conditional probability of $\omega_{tk} = 1$, given $\boldsymbol{\omega}_{t-1-d}^{t-1}$, is specified as

$$\mathbb{P}[\omega_{tk} = 1 | \boldsymbol{\omega}_{t-1-d}^{t-1}] = \beta_k + \sum_{s=1}^d \sum_{l=1}^K \beta_{kl}^s \omega_{(t-s)l}, 1 \leq k \leq K. \quad (1)$$

The model parameters can also be interpreted and understood as follows:

- β_k denotes the intrinsic probability of abnormality at the k -th location, without any exogenous influence from the past periods and from other locations. It is also called the birthrate.
- β_{kl}^s denotes the magnitude of influence on location k and time t of the event occurred at time $t - s$ and location l . The sum captures the *cumulative influence* up to time $t - 1$ from all the other locations to the current location at time t .

This conditional probability model explicitly captures the dependence of event at time t and location k on events from all locations in the past d days. The set of model parameters are $\boldsymbol{\beta} = \{\beta_k, \beta_{k\ell}^s : 1 \leq s \leq d, 1 \leq k, \ell \leq K\}$. Define the number of parameters $\kappa := K^2d + K$, then $\boldsymbol{\beta} \in \mathbb{R}^\kappa$.

To ensure (1) returns reasonable probabilities, we require that parameters belong to the set:

$$\mathcal{X} := \left\{ \boldsymbol{\beta} : \begin{array}{l} 0 \leq \beta_k + \sum_{s=1}^d \sum_{\ell=1}^K \min[\beta_{k\ell}^s, 0], \forall k \leq K \\ 1 \geq \beta_k + \sum_{s=1}^d \sum_{\ell=1}^K \max[\beta_{k\ell}^s, 0], \forall k \leq K \end{array} \right\}. \quad (2)$$

Remark 1 (Complexity of the algorithm). The complexity to solve the problem is high when K is large. In such case, sparsity can be imposed in this model. For example, we may assume that a pair of locations has no influence on each other if the distance between them is larger than a threshold, without losing the convexity of (1).

Multi-state model: We can naturally extend the above model to a M -state process. Keeping the same notations with minor modifications, our observed data are denoted as $\omega^T = \{\omega_{tk}, 1 \leq t \leq T, 1 \leq k \leq K\}$, where $\omega_{tk} \in \{0, 1, \dots, M\}$. Given a memory window d , define $\omega_{t-d}^t = \{\omega_{sk}, t-d \leq s \leq t, 1 \leq k \leq K\}$. Thus, the only difference from the single-state model is that we allow the random variables ω_{tk} to be categorical rather than binary. For each location k , we associate an array of baseline parameters $\bar{\beta}_k = \{\bar{\beta}_k(p), 1 \leq p \leq M\}$, and for every pair of locations k, l and every $s \in \{1, \dots, d\}$, an array of interaction parameters $\bar{\beta}_{kl}^s = \{\bar{\beta}_{kl}^s(p, q), 1 \leq p \leq M, 0 \leq q \leq M\}$. Thus, for each category $p \in \{1, \dots, M\}$, the conditional probability is written as

$$\mathbb{P}[\omega_{tk} = p | \omega_{t-1-d}^{t-1}] = \bar{\beta}_k(p) + \sum_{s=1}^d \sum_{\ell=1}^K \bar{\beta}_{k\ell}^s(p, \omega_{(t-s)\ell}), \quad (3)$$

$$\text{and } \mathbb{P}[\omega_{tk} = 0 | \omega_{t-1-d}^{t-1}] = 1 - \sum_{p=1}^M \left[\bar{\beta}_k(p) + \sum_{s=1}^d \sum_{\ell=1}^K \bar{\beta}_{k\ell}^s(p, \omega_{(t-s)\ell}) \right].$$

The parameters have similar interpretations as those in the single-state model and the number of parameters in this model is $\kappa := KM + K^2dM(M+1)$. Similarly, to ensure (3) outputs reasonable probabilities, we require that parameters belong to the following set:

$$\mathcal{X} := \left\{ \beta : \begin{array}{l} 0 \leq \bar{\beta}_k(p) + \sum_{s=1}^d \sum_{\ell=1}^K \min_{0 \leq q \leq M} \bar{\beta}_{k\ell}^s(p, q), 1 \leq p \leq M, 1 \leq k \leq K, \\ 1 \geq \sum_{p=1}^M \bar{\beta}_k(p) + \sum_{s=1}^d \sum_{\ell=1}^K \max_{0 \leq q \leq M} \bar{\beta}_{k\ell}^s(p, q), 1 \leq k \leq K. \end{array} \right\} \quad (4)$$

3 Model estimation and prediction

In this section, we introduced the main algorithms for both model estimation and prediction separately. First, we elaborate on the Least-Square method and the Maximum Likelihood method for parameter estimation. We give theoretical guarantees on estimates from both methods. We propose an online ramping event prediction method that works for non-stationary time-series by comparing estimated ramping probabilities with carefully designed dynamic thresholds.

3.1 Least-Square (LS) method

Given a sequence of observations $\mathbf{x}^T = \{x_{ts}, 1 \leq t \leq T, 1 \leq s \leq K\}$, we first transform them into single-state or multi-state abnormal events $\omega^T = \{\omega_{ts}, 1 \leq t \leq T, 1 \leq s \leq K\}$ as in Section 2.1. Based on the conditional probability model proposed in Section 2.2, we can estimate the model parameters β by minimizing the sum-of-square errors between conditional probabilities and extracted abnormal events. This leads to the following single-state and multi-state optimization problems. For single-state modeling, we consider the objective

$$\Psi_{\omega^N}(\beta) = \frac{1}{2N} \sum_{t=1}^N \sum_{k=1}^K \left((\beta_k + \sum_{s=1}^d \sum_{\ell=1}^K \beta_{k\ell}^s \omega_{(t-s)\ell}) - \omega_{tk} \right)^2, \quad \omega_{tk} \in \{0, 1\}. \quad (5)$$

For multi-state modeling, we consider the objective

$$\Psi_{\omega^N}(\hat{\beta}) = \frac{1}{2N} \sum_{t=1}^N \sum_{k=1}^K \left\| \left(\bar{\beta}_k + \sum_{s=1}^d \sum_{\ell=1}^K \bar{\beta}_{k\ell}^s (\omega_{(t-s)\ell}) \right) - \bar{\omega}_{tk} \right\|_2^2, \quad \omega_{(t-s)\ell} \in \{0, 1, \dots, M\}. \quad (6)$$

In (6), $\bar{\omega}_{tk} := e_{\omega_{tk}} \in \mathbb{R}^M$ is the M -state abnormal vector, whose i^{th} entry is 0 if ω_{tk} is in state $i > 0$, and is the zero vector if $\omega_{tk} = 0$. This vector encodes the true state of the data point at time t and location k . Also, $\bar{\beta}_k = \{\bar{\beta}_k(p) \in \mathbb{R}, p \in \{1, \dots, M\}\} \in \mathbb{R}^M$ and $\bar{\beta}_{kl}^s(\omega_{(t-s)\ell}) = \{\bar{\beta}_{kl}^s(p, \omega_{(t-s)\ell}) \in \mathbb{R}, p \in \{1, \dots, M\}\} \in \mathbb{R}^M$.

Thus, the problem of recovering parameters β can be formulated as solving the following constrained convex optimization problem as stated in [19], where the constraints sets \mathcal{X} are previously specified in (2) (single-state) and (4) (multi-state):

$$\hat{\beta}(\omega^N) := \arg \min_{\beta \in \mathcal{X}} \Psi_{\omega^N}(\beta). \quad (7)$$

Note this optimization problem has a strongly convex objective function (the least-square cost function), and it can be solved efficiently in polynomial time.

We also show the performance guarantee of our estimator $\hat{\beta}$. For notation simplicity, we first define function $\eta(\cdot)$ on the set of all zero-one arrays $\omega_{t-d}^{t-1} \in \{0, 1\}^{d \times K}$ that takes values in the matrix space $\mathbb{R}^{K \times \kappa}$:

$$\eta^\top(\omega_{t-d}^{t-1}) = [I_K, I_K \otimes \text{vec}(\omega_{t-d}^{t-1})^\top] \in \mathbb{R}^{K \times \kappa}, \quad (8)$$

where I_K is K -dimensional identity matrix, \otimes denotes the standard Kronecker product, $\text{vec}(\cdot)$ vectorizes a matrix by stacking all columns. Now define the empirical regret function for parameter recovery as:

$$F_{\omega^N}(x) = \left[\frac{1}{N} \sum_{t=1}^N \eta(\omega_{t-d}^{t-1}) \eta^\top(\omega_{t-d}^{t-1}) \right] x - \frac{1}{N} \sum_{t=1}^N \eta(\omega_{t-d}^{t-1}) \omega_t, \quad (9)$$

which is shown in [19] to be monotone and affine. Also, we define

$$A[\omega^n] := \frac{1}{N} \sum_{t=1}^N \eta(\omega_{t-d}^{t-1}) \eta^\top(\omega_{t-d}^{t-1}),$$

and the condition number given $A \in \mathbb{R}^{\kappa \times \kappa}$, $A \succ 0$:

$$\theta_p[A] := \max\{\theta \geq 0 : g^\top A g \geq \theta \|g\|_p^2, \forall g \in \mathbb{R}^\kappa, p \in [1, \infty]\}. \quad (10)$$

Finally we can bound estimation error for the above LS estimates by utilizing concentration inequalities for martingales.

Theorem 3.1 (Bounding ℓ_p error of LS estimate [19]). *For every $p \in [1, \infty]$ and every ω^N one has*

$$\|\hat{\beta}(\omega^N) - \beta\|_p \leq \|F_{\omega^N}(\beta)\|_\infty / \sqrt{\theta_p[A[\omega^N]] \theta_1[A[\omega^N]]}. \quad (11)$$

With bounds on $\|F_{\omega^N}(\beta)\|_\infty$, it can be shown that for every $\epsilon \in (0, 1)$ and any $p \in [1, \infty]$, the probability of the event

$$\|\hat{\beta}(\omega^N) - \beta\|_p \leq \left(\sqrt{\frac{\ln(2\kappa/\epsilon)}{2N}} + \frac{\ln(2\kappa/\epsilon)}{3N} \right) / \sqrt{\theta_p[A[\omega^N]] \theta_1[A[\omega^N]]}, \quad (12)$$

is at least $1 - \epsilon$.

Remark 2. The quantity $\theta_p[A[\omega^N]]$ is readily computable when $p = 2$ or ∞ : it is the minimum eigenvalue when $p = 2$ and it is $\min_{1 \leq i \leq \kappa} \{x^T A x : \|x\|_\infty \leq 1, x_i = 1\}$ when $p = \infty$, which is the minimum of κ efficiently computable quantities. Solving for $p = 1$ is hard in general. However, it is argued in [19] that upon passing to polars, one can solve for the semidefinite relaxation upper bound on $\max_{\|x\|_\infty \leq 1} x^T Q x$ for $Q := A^{-1}$ by

$$\min_{\lambda} \left\{ \sum_i \lambda_i : \lambda_i \geq 0, \forall i; \text{Diag}\{\lambda_1, \dots, \lambda_\kappa\} \succeq Q \right\},$$

which is tight within the factor $\pi/2$ [25]. Borrowing the remark on page 11 of [19], we can expect that the minimum eigenvalue of $A[\omega^n]$ will be of order 1 with high probability, so that the bound using (12) goes to 0 as $N \rightarrow \infty$ at the rate $O(1/\sqrt{N})$. As a result, $\hat{\beta} \xrightarrow{p} \beta$.

Also, we note that all the data-driven parameters in (12) are computable given ramping event data. We will show numerical values of these bounds under different norms in the Experiment Section 4.

3.2 Maximum-Likelihood (ML) method

Another method we use for recovery of the parameters is the Maximum-Likelihood (ML) method. Following [19], we additionally assume that for every t , random variables ω_{tk} are conditionally independent across locations k given the past history $\boldsymbol{\omega}^{t-1}$, so that conditional probabilities are separable. Below are definitions of the likelihood objective functions for the proposed model in both single and multi-state cases.

For the single-state model, the negative log-likelihood function (conditioned on the value of ω^0) is:

$$L(\boldsymbol{\beta}) = \frac{1}{N} \sum_{t=1}^N \sum_{k=1}^K \left[-\omega_{tk} \ln \left(\beta_k + \sum_{l=1}^k \sum_{s=1}^d \beta_{kl}^s \omega_{(t-s)l} \right) - (1 - \omega_{tk}) \ln \left(1 - \beta_k - \sum_{l=1}^k \sum_{s=1}^d \beta_{kl}^s \omega_{(t-s)l} \right) \right]. \quad (13)$$

For multi-state model with M states, we follow notations from the least-square subsection to form the following objective function:

$$L(\boldsymbol{\beta}) = -\frac{1}{N} \sum_{t=1}^N \sum_{k=1}^K \psi_{tk}(\bar{\boldsymbol{\beta}}_k, \boldsymbol{\omega}^N), \quad (14)$$

where

$$\psi_{tk}(\bar{\boldsymbol{\beta}}_k, \boldsymbol{\omega}^N) = \begin{cases} \ln \left(\bar{\beta}_k(p) + \sum_{s=1}^d \sum_{l=1}^K \bar{\beta}_{kl}^s(p, \omega_{(t-s)l}) \right), & \omega_{tk} = p > 0 \\ \ln \left(1 - \sum_{p=1}^M \left(\bar{\beta}_k(p) + \sum_{s=1}^d \sum_{l=1}^K \bar{\beta}_{kl}^s(p, \omega_{(t-s)l}) \right) \right), & \omega_{tk} = 0 \end{cases}$$

We call a minimizer vector $\hat{\boldsymbol{\beta}}$ of (13) or (14), subject to the same constraints in (2) (single-state) or (4) (multi-state), the maximum likelihood (ML) estimate:

$$\hat{\boldsymbol{\beta}} = \arg \min_{\boldsymbol{\beta} \in \mathcal{X}} L(\boldsymbol{\beta}).$$

It can be verified that the objective function is convex since it resembles the likelihood function for generalized linear model (GLM) with Bernoulli link functions. Thus it can be solved efficiently by convex optimization algorithms as we did for LS estimates.

The gradient of ML objective can be derived as

$$F_{\omega^N}(\boldsymbol{\beta}) = \nabla L(\boldsymbol{\beta}) = \frac{1}{N} \sum_{t=1}^N \eta(\omega_{t-d}^{t-1}) \theta(\eta^T(\omega_{t-d}^{t-1}) x, \omega_t),$$

where

$$\theta(z, \omega) = \nabla_z \mathcal{L}_\omega(z) = - \sum_{k=1}^K \left[\sum_{p=1}^M \frac{[w]_{kp}}{[z]_{kp}} e^{kp} - \frac{1 - \sum_{p=1}^M [w]_{kp}}{1 - \sum_{p=1}^M [z]_{kp}} \sum_{p=1}^M e^{kp} \right], \quad [w \in Z_0]$$

$$Z_0 = \left\{ \omega \in \mathbf{R}^{MK} : \omega \geq 0, \sum_{p=1}^M [\omega]_{kp} \leq 1, \forall k \leq K \right\}.$$

To make sure $F_{\omega^N}(\boldsymbol{\beta})$ is continuous, we also require $\boldsymbol{\beta} \in B_\rho$, for B_ρ being a ρ -strengthened version of constraints (4) as follows:

$$B_\rho := \left\{ \begin{array}{l} \varrho \leq \beta_k(p) + \sum_{s=1}^d \sum_{\ell=1}^K \min_{0 \leq q \leq M} \beta_{k\ell}^s(p, q), 1 \leq p \leq M, 1 \leq k \leq K \\ 1 - \varrho \geq \sum_{p=1}^{M-1} \beta_k(p) + \sum_{s=1}^d \sum_{\ell=1}^K \max_{0 \leq q \leq M} \beta_{k\ell}^s(p, q), 1 \leq k \leq K \end{array} \right\}. \quad (15)$$

Below is the bound on the l_∞ norm of $F_{\omega^N}(\boldsymbol{\beta})$ that allow us to analyze the performance guarantee of our estimate $\hat{\boldsymbol{\beta}}$.

Lemma 3.2. For all $\epsilon \in (0, 1)$ vector $F_{\omega^N}(\boldsymbol{\beta})$ satisfies

$$\text{Prob}_{\omega^N} \left\{ \|F_{\omega^N}(\boldsymbol{\beta})\|_\infty \geq \frac{1}{\rho} \sqrt{\frac{2 \ln(2\kappa/\epsilon)}{N}} \right\} \leq \epsilon, \rho \in (0, 1)$$

The proof details of lemma 3.2 can be found in appendix. We can use lemma 3.2 and $\theta_p(A)$, which is defined in (10) to provide bound on $\|\hat{\beta} - \beta\|_p$, as in the following theorem, whose proof also appear in the appendix:

Theorem 3.3. *For every $p \in [1, \infty]$ and every ω^N one has*

$$\|\hat{\beta} - \beta\|_p \leq (1 - \rho)^2 \|F_{\omega^N}(\beta)\|_\infty / \sqrt{\theta_1(A)\theta_p(A)}.$$

As a result, given any $\rho \in (0, 1)$ and $\epsilon \in (0, 1)$, the probability of the event

$$\|\hat{\beta} - \beta\|_p \leq \frac{(1 - \rho)^2}{\rho} \sqrt{\frac{2 \ln(2\kappa/\epsilon)}{N}} / \sqrt{\theta_1(A)\theta_p(A)} \quad (16)$$

is at least $1 - \epsilon$.

3.3 Sequential anomaly event prediction

Given a set of single-state or multi-state estimates $\hat{\beta}$ for parameters β , we can calculate the conditional probability of ω_{tk} at any state, location, and time using our single-state model (1) or multi-state model (3). For example, the predicted probability of being abnormal in single-state modeling using $\{\omega_{tk}\}$ is

$$\hat{p}_{tk} := \hat{\beta}_k + \sum_{s=1}^d \sum_{l=1}^K \hat{\beta}_{kl}^s \omega_{(t-s)l}.$$

We make sequential prediction on future conditional probabilities using the estimated parameters $\hat{\beta}$, data from the past d days, using (1) or (3). Thus, our prediction mechanism assumes that we can observe future data sequentially after prediction and thus incorporate this new information into prediction. Then, we use the sequentially estimated probability to detect abnormal events. For each location k and each future time index t , $\hat{\omega}_{t,k} = 1$ if $\hat{p}_{tk} \geq \tau_{tk}$ and 0 otherwise. The set of abnormal thresholds $\{\tau_{tk}\}$ can be defined sequentially and dynamically or be fixed in advance. We note that appropriate choices of τ_{tk} would help us effectively addressing non-stationarity in prediction.

3.3.1 Choice of threshold

In this section, we discuss an important parameter, the threshold in using probability calculated from our estimated model.

Static threshold: At a given location k , we can set $\tau_{tk} = \tau_k$ for all t and τ_k is determined and fixed before predictions (such as via cross-validations). This procedure produces static thresholds. However, determining a proper threshold is not an easy task since it is very sensitive to problem settings.

Dynamic threshold: To make the algorithm more robust and flexible, we adjust τ_{tk} at a given location k dynamically to fit different patterns of anomalies. Define w_2 as the pre-determined window size, so the online threshold can be adjusted using the sliding window which contains the past observed events $(\omega_{t-1-d_2}^{t-1})_k$ and the past predicted probability $(\hat{p}_{t-1-d_2}^{t-1})_k$. Thus, the current threshold can be defined as the weighted average of the data points inside the sliding window:

$$\tau_{tk} = \alpha \frac{\sum_{i=1}^{w_2} \hat{p}_{(t-i)k} \omega_{(t-i)k}}{\sum_{i=1}^{w_2} \omega_{(t-i)k}} + (1 - \alpha) \frac{\sum_{i=1}^{w_2} \hat{p}_{(t-i)k} (1 - \omega_{(t-i)k})}{w_2 - \sum_{i=1}^{w_2} \omega_{(t-i)k}}, \quad t \geq w_2, \quad (17)$$

where $\alpha \in (0, 1)$ is a predefined parameter, which determines the distance between the detecting threshold and the normal or abnormal events. If α is close to 0, the threshold will tend to treat more events as abnormal, while a large α will set a high standard for detecting an anomaly, resulting in fewer abnormal events. Thus the trade-off between these two scenarios can be balanced by adjusting α .

The intuition for choosing this threshold is that we aim to find the best middle point between normal and abnormal history events within a time sliding window, and the current decision is made based on this

online middle point. The choice of the parameter d_2 determines “memory-length”. In the experiments, we will show that prediction using dynamic thresholds is better than predictions using static thresholds in these non-stationary time-variant series.

The definition can be naturally extended to multi-state cases. For an M -state case, the dynamic threshold $\tau_{tk}^{(i)}$ which separates state $i - 1$ and i can be calculated through:

$$\tau_{tk}^{(i)} = \frac{i}{M+1} \sum_{m=1}^M \frac{\sum_{i=1}^{w_2} \hat{p}_{(t-i)k} \mathbb{1}(\omega_{(t-i)k} = m)}{\sum_{i=1}^{w_2} \mathbb{1}(\omega_{(t-i)k} = m)}, \quad t \geq w_2, i = 1, \dots, M. \quad (18)$$

Note that if $\sum_{i=1}^{w_2} \mathbb{1}(\omega_{(t-i)k} = m) = 0$, we will have 0/0 in the corresponding term. In this case, we will let the dynamic threshold be the static threshold found via cross-validation. Same strategy is used in (17).

3.3.2 Prediction interval

We build bootstrap confidence intervals for parameters β as follows: for each $b = 1, \dots, 100$, we re-sample uniformly with replacement from $\{\omega_{tk}\}$ to create $\{\omega_{tk}^b\}$. Then, we fit $\hat{\beta}^b$ using our earlier models and data $\{\omega_{tk}^b\}$ and calculate standard errors for each component of β using the 100 bootstrap estimates; for notation simplicity, we write the standard error vector as SE_{boot} , which has the same dimension as β . Finally, we form the $1 - \epsilon$ confidence interval for β as $\hat{\beta} \pm z_{1-\epsilon/2\kappa} SE_{boot}$. z_α is the α -quantile of a $N(0, 1)$ random variable. Note we use the conservative Bonferroni correction here in the multiplier $z_{1-\epsilon/2\kappa}$, because we want to make sure the intervals are valid for all the components of β . We choose $\epsilon = 0.05$. We then build confidence intervals for ramp event probabilities using our models and the confidence intervals for β calculated above. Specifically, the upper end of confidence intervals for probabilities are calculated using $\hat{\beta} + z_{1-\epsilon/2\kappa} SE_{boot}$ and lower end using $\hat{\beta} - z_{1-\epsilon/2\kappa} SE_{boot}$.

4 Real-data study

In this section, we first explore the dataset we use in Section 4.1. Then, we start with single-state ramping event modeling in Section 4.2, where we first discuss the choice of hyperparameters, then visualize and analyze the estimated model parameters. We also implement numerical experiments to verify the correctness of performance guarantees by earlier theorems. Finally, for single-state estimation, we present the prediction performance by using different choices of the threshold. We then focus on modeling multi-state anomaly events in Section 4.3 by using similar approaches for single state cases. Here, we consider two non-zeros states, +1 as a positive ramping event and -1 as a negative ramping event. In the end, we fit two separate models in summer and winter in Section 4.4 and show our model well captures seasonal differences.

4.1 Dataset Description

We retrieve from the NSRDB¹ website 2017 and 2018 bi-hourly solar radiation data, collected every day from sensors across different states and cities in the US. Sensors can be located using longitudes and latitudes. The 2017 data are used for estimating β in our model and 2018 for sequential prediction. Specifically, we collect three sets of such data: two uniform 3-by-3 grids of data, which center at downtown Atlanta or downtown Los Angeles and each pair of grids points (i.e., sensors) with the same longitude and latitude are separated by 0.076-degree (5 miles), and a non-uniform set of 10 downtown data across different cities² in California. We choose these places because of the weather differences among them. Thus we can demonstrate the flexibility of our model. We visualize the two sets of sensor locations on the map in Figure 3.

We briefly describe the structure of these data: there are 48 recordings at a location for any given day so that two consecutive recordings are 30 minutes apart. Each bi-hourly recording contains a row of radiation values, including Global Horizontal Irradiance (GHI), Direct Normal Irradiance (DNI), and Diffuse

¹dataset available at <https://nsrdb.nrel.gov/>

²Complete list of cities: Fremont, Milpitas, Mountain View, North San Jose, Palo Alto, Redwood City, San Mateo, Santa Clara, South San Jose, Sunnyvale

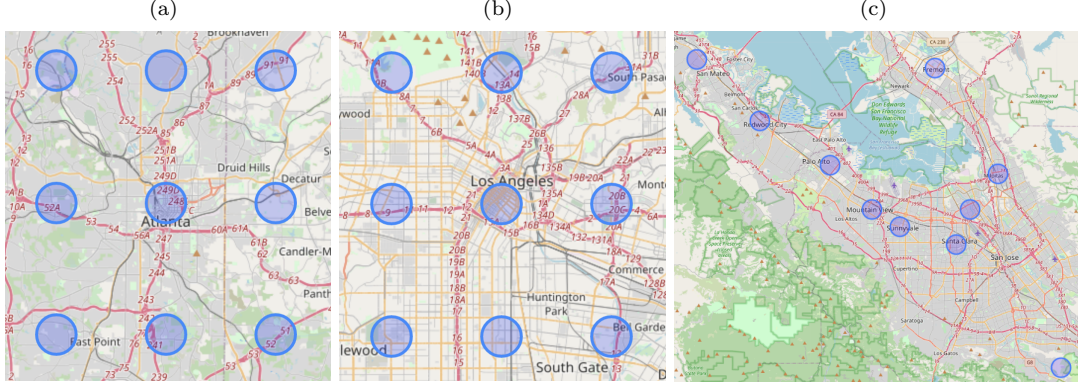


Figure 3: Locations where the 2017-18 raw radiation data are collected: (a) 9 locations near downtown Atlanta, (b) 9 locations around downtown Los Angeles, (c) 10 downtown of different cities in Northern California. Each pair of locations along the same longitude or magnitude in (a) and (b) are 0.076 degree (5 miles) apart.

Horizontal Irradiance (DHI), which reflect radiation levels, and various other features such as wind speed, temperature, solar zenith angle, etc. Since the GHI is correlated with the other two metrics as:

$$\text{GHI} = \text{DNI} \cdot \cos(\theta) + \text{DHI},$$

where θ is the solar zenith angle, we use GHI mainly to extract single-state and multi-state abnormal events as follows: we define $\{x_{tk}\}$ as the set of daily average of solar radiations at day t , $1 \leq t \leq 365$ and $1 \leq k \leq 9$ for Atlanta or Los Angeles or $1 \leq k \leq 10$ for California. Then, we use the technique in Section 2.1 to extract $\{\omega_{tk}\}$. How we pick the parameters are described in Section 4.2.1.

Before modeling, we visualize and compare the trends of 2017 GHI values in Atlanta, Palo Alto (Northern California), Los Angeles (South California). The trends of 2017 DHI and DNI are similar. We provide a set of three raw GHI plots at 8:30 am, 12:00 pm, and 16:30 pm over the whole year. Figure 4 shows volatile fluctuations in daily recordings at a specific time, with similar peak values during June till August. In particular, GHI values in Californian cities are typically higher than that in Atlanta during mornings but generally are lower during late afternoons.

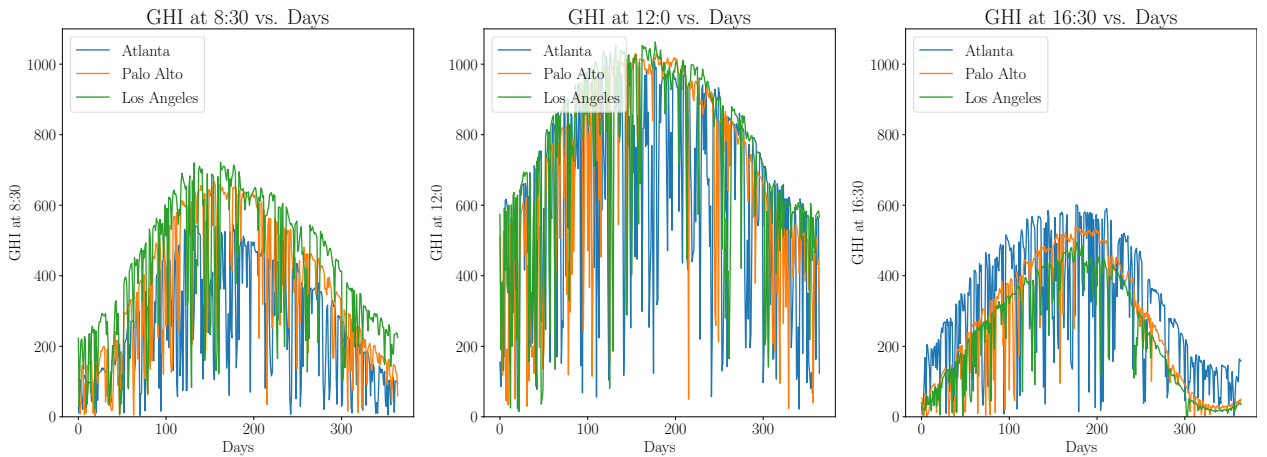


Figure 4: 2017 Raw data at different time during the day over 365 days. We observe clear non-stationarity in all series. Observations in Atlanta have lower radiation levels than those in California in the morning (8:30 AM) and at noon (12:00 PM), but have higher values in late afternoon (4:30 PM).

4.2 Single-state ramping event extraction

In this section, we provide the following results upon using our model: the choice of hyperparameters is discussed in Section 4.2.1. In Section 4.2.2 and Section 4.2.3, we show parameter recovery results by plotting recovered β over locations and time and by plotting these parameters on terrain map for more meaningful analysis. Then we verify the tightness of performance guarantee (Theorem 3.1) by conducting several numerical experiments in Section 4.2.4. Finally, in Section 4.2.5, we examine the prediction performance of our model under static vs. dynamic threshold, first by showing average frequency prediction results and then by analyzing prediction performance in terms of precision, recall, and F_1 score, as we plot sequential point predictions under static and dynamic thresholds.

4.2.1 Choice of hyperparameters

The hyperparameters in the experiments include the window size w_1 and the quantile of threshold δ for extracting the ramping events, memory depth d in the Bernoulli model, the window length w_2 and adjusting factor α for updating dynamic threshold for online anomaly detection. We will firstly show how we deal with these hyperparameters in the experiment.

The window size w_1 is set to be 30, which means we consider the history observations for up to one month, which makes sense since the different seasons will have different solar radiation patterns; thus, setting a larger size will not be accurate. Moreover, it is not robust for setting a smaller window size since we may have quite noisy observations in a short time length like a rainstorm that persists for one week.

The choice of δ is more tricky. Thus we perform a test by calculating the Mean Square Error (MSE) for frequency test under different choices of δ , and we see from Figure 5 that the results are sensitive to this parameter and have a minimum value when $\delta = 0.0005$. For the memory depth d , we tune it after we recover

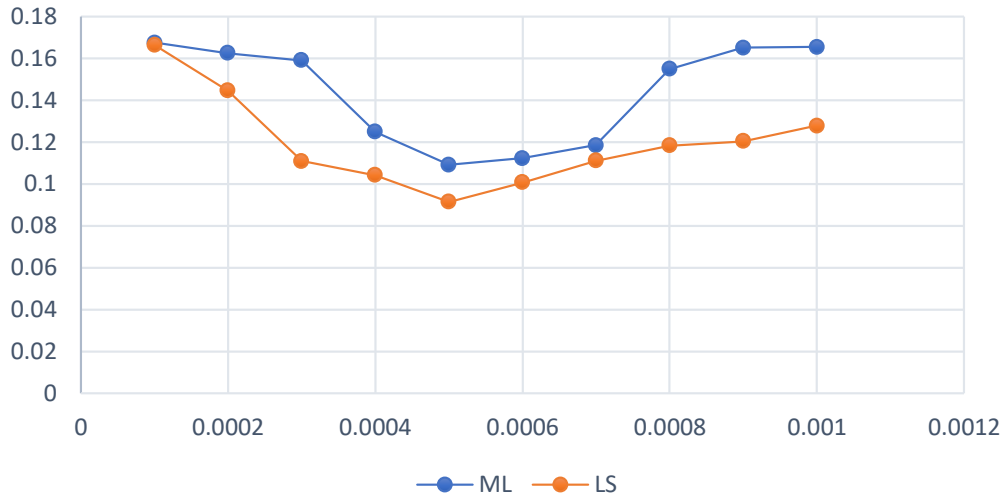


Figure 5: Choice of δ by comparing MSE of the frequency test for estimation of frequency under the proposed Bernoulli model.

the spatial-temporal influence. In most cases, the temporal influence declines dramatically with the increase of memory depth. We observe that $d = 10$ is a reasonable choice since the temporal influence between any arbitrary locations declines to around 0 when $d > 10$.

As for the hyperparameters appeared in online threshold update for anomaly detection in Section 3.3, we set the first 30% data for tuning both static thresholds and w_2 used in dynamic thresholds and the last 70% data for testing with the tuned parameters. We tuned the best w_2 over a 25 uniformly spaced w_2 from 10 to 110 and α from 0.1 to 0.9. Finally we empirically choose $\alpha = 0.5$ and $w_2 = 50$.

4.2.2 Recovered spatial-temporal influence

Figure 6 shows the recovered single-state baseline parameters β_k over different location and a selected number of interaction parameters β_{kl}^s over time. Bootstrap confidence intervals as discussed in Section 3.3 are plotted around estimates. We can see that the magnitude of birthrate estimates is similar between LA and North California (CA), and birthrates in Atlanta (ATL) are the smallest among all three, likely because California is sunnier than Atlanta, so that radiation levels are higher in California. Interaction estimates between different sensors decay very fast regardless of location, indicating location-to-location influences do not persist over time. Estimates recovered by ML and LS are, in general very similar.

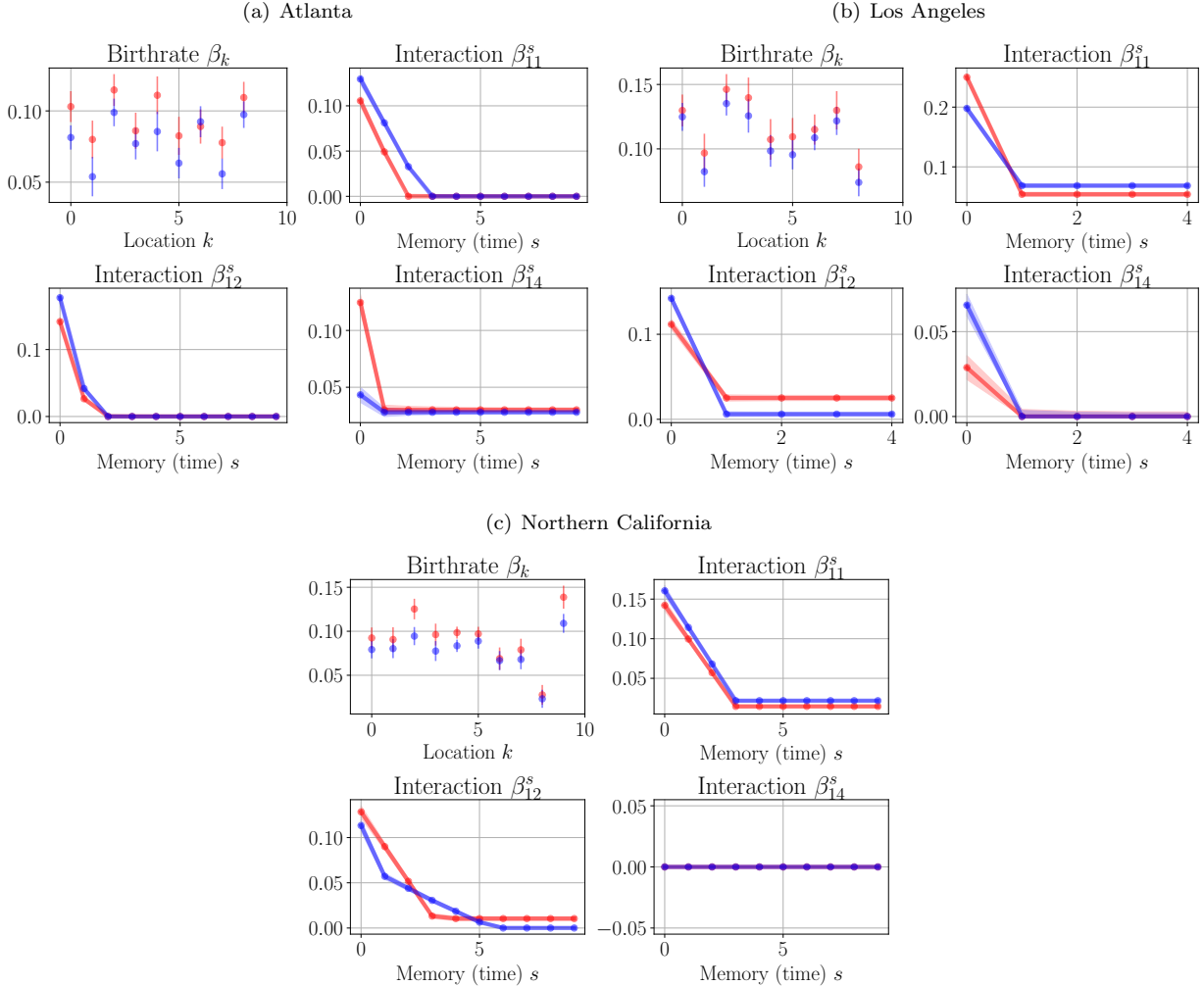


Figure 6: Recovered birthrate parameters at different locations and interaction parameters over time. The blue curve shows ML recoveries, and the red curve shows LS recoveries. The shaded areas are 95% confidence intervals under bootstrap. Birthrates are similar in magnitude across different locations, and interactions all decay very fast over time.

4.2.3 Visualize influence parameters on terrain map

To better visualize and analyze the influences in reality, we plot these parameters as graphs on terrain map. Only maximum likelihood estimates are shown here; the estimates using LS are given in the appendix. The size of vertices and width of edges are proportional to the magnitude of corresponding recovered parameters. From Figure 7, we can find the following temporal patterns over time at each location:

- In Atlanta, birthrates are stronger in the corner. Regarding influence parameters, at $s = 1$, interactions have relatively uniform magnitude, so every pair of neighboring sensors interacts with each other. We find more latitude-wise (vertical) interactions than longitude-wise (horizontal) ones as well. At $s = 5$ and 10, it influences decay in magnitude, but those in the west and east of downtown maintain the magnitude compared to other influences.
- In Los Angeles, the birthrate is stronger on the west side and north side of downtown. Regarding influence parameters, at $s = 1$, interactions are more obvious along latitude than along longitude. We also see compatible magnitudes on the south side of downtown. At $s = 3$ and 5, influences that are strong at the beginning tend to persist. We still see more along latitude than longitude and active interactions among sensors.
- In Northern California, birthrates are very similar in size and concentrate around the northwest side of the map. Regarding influence parameters, at $s = 1$, we see strong influences from a city onto itself. In addition, influences flow towards south east mainly, and connections can be strong even if cities are far away (such as San Mateo to Santa Clara and Sunnyvale to South San Jose). At $s = 5$ and 10, influences follow almost the same directions with decreasing magnitude.

Spatially, as we compare the two uniform grids of sensors at ATL and LA, we see that they have similar interactions (in terms of magnitude), but birthrates in ATL are smaller than those in LA. We suspect large birthrate magnitude under similar sensor interactions would lead to a higher average frequency of ramping events in LA than in ATL. We will observe this phenomenon in the next subsection. On the other hand, it is harder to compare either Atlanta or Los Angeles results with Northern California results due to how sensors are located. Nevertheless, we can see that birthrate magnitudes and strengths of interactions are similar between Northern California cities and Los Angeles, and both results are stronger than Atlanta’s results. Although we can generally expect this situation to occur due to closer geographic proximity between Northern California and Los Angeles, it is interesting to be able to quantitatively and intuitively analyze this situation.

4.2.4 Empirical examination of performance guarantee of estimates

Using data from Atlanta, Los Angeles, and Northern California, we can compute the norm bound under $p = 1, 2, \infty$ efficiently and therefore provide the bound numerical values as mentioned in (12). Table 2 presents the results under these three choices of the norm. Here, $\kappa = K + dK^2$, $N = 365$, and we choose $\epsilon = 0.1$. We can see from the table that increasing p leads to a larger condition number and, as a result, a tighter bound around the norm of differences. We notice that the condition number for Northern California when $p = 2$ is 0, which is because the norm of the minimal eigenvalue of $A[\omega^N]$ under that case is 0 under rounding to five decimal places.

Table 2: Condition number $\theta_p(A[\omega^n])$ and the resulting bounds on $\|\hat{\beta} - \beta\|_p$ from $p = 1, 2, \infty$, using Theorem 3.1.

Location	$\theta_1(A[\omega^n])$	$p = 1$		$p = 2$		$p = \infty$	
		Bound on $\ \hat{\beta} - \beta\ _1$	$\theta_2(A[\omega^n])$	Bound on $\ \hat{\beta} - \beta\ _2$	$\theta_\infty(A[\omega^n])$	Bound on $\ \hat{\beta} - \beta\ _\infty$	
Atlanta	9e-05	24.53408	0.00668	2.84776	0.29315	0.42988	
Los Angeles	1.6e-04	15.23908	0.01175	1.77828	0.4274	0.29485	
North California	3e-05	35.89018	0.0	∞	0.41096	0.30665	

4.2.5 Prediction performance

Using techniques in Section 3.3, we make a sequential prediction for Downtown Atlanta, Downtown Los Angeles, and Palo Alto (Northern California). When choosing dynamic threshold values, whenever $1 \leq t \leq w_2$ or there is no abnormal event in the memory window of length w_2 , we set the dynamic threshold to be the best static threshold that maximizes F_1 score on the validation data. Then, we calculate average

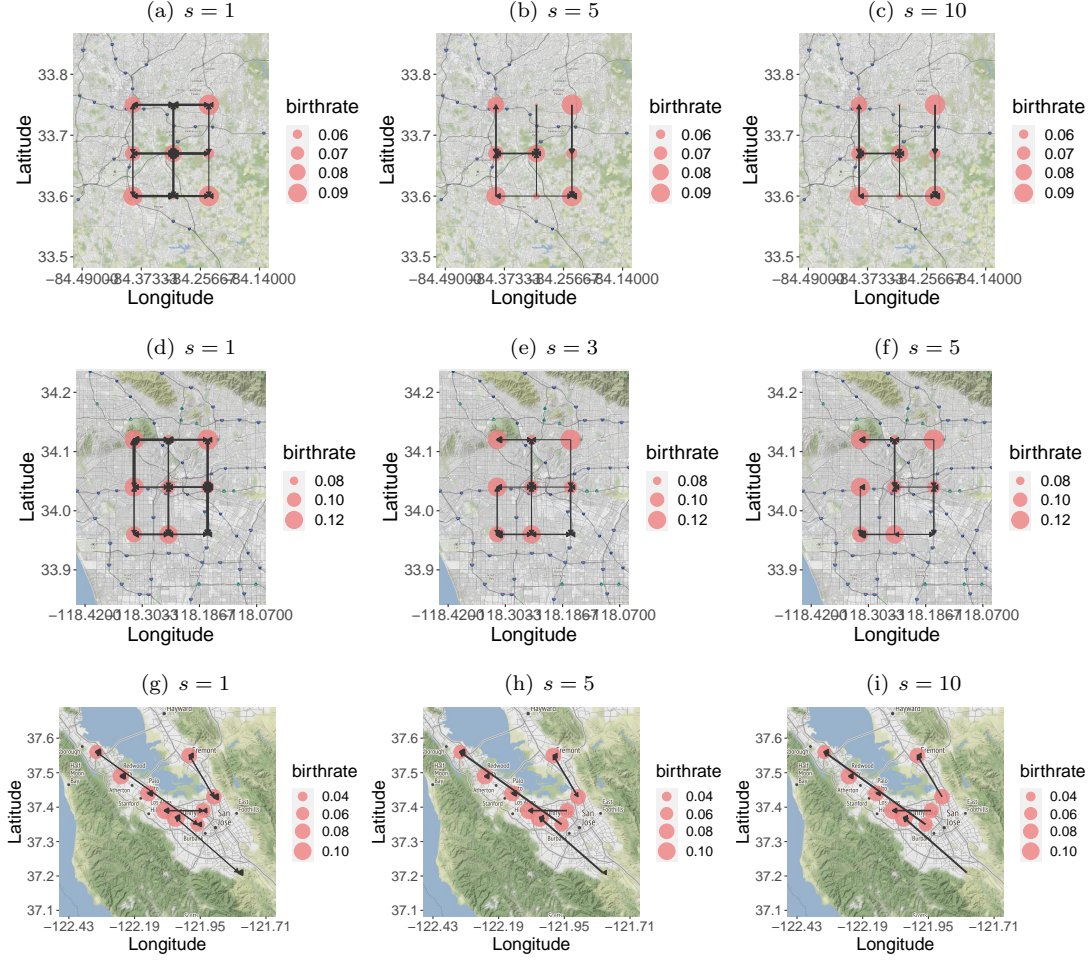


Figure 7: Visualization of ML birthrate (red circles) and interactions (black lines) recovery (shown in Figure 6 over time and locations) on terrain map. To make sure the edges are visible when $s > 1$, we magnify the edge weight of Atlanta (a-c) and Northern California (g-i) estimates 5 times, and Los Angeles (d-f) estimates 3 times.

ramping event frequency from our predictions using static and dynamic thresholds as a crude measure of performance and compare with the truth average ramping event frequency. The comparisons are shown in Figure 8, from which we can make two observations. First, there are significant differences between the frequency of ramping events at these locations, and our model can recover the ground truth frequency in some cases. Second, due to the non-stationarity of our data, predictions under a dynamic threshold are closer to the ground truth.

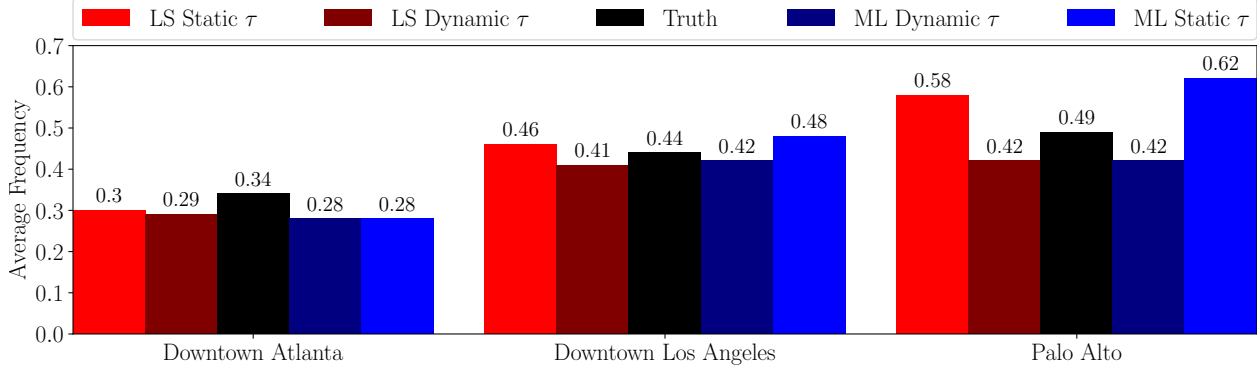


Figure 8: Average frequency of predicted (red and blue bars) vs. actual (black bars) abnormal events at different downtown locations for both LS and ML method. Predictions under dynamic thresholds are in general closer to the actual values than those under static thresholds.

To examine model prediction performance in greater detail, we compute precision, recall, and F_1 score³ as three metrics, using static and dynamic thresholds proposed in Section 3.3. The details are recorded in Table 3. We show how we tune the best static threshold τ in Figure 9, in which we searched over a grid of 25 uniformly spaced τ in $[0, 1]$ and use τ with the highest F_1 score as the static τ in Table 3. Also, we plot the point predictions and static/dynamic thresholds with confidence intervals in Figure 10 to better show how we make the predictions for the last 70% of data. Figure 9 shows that the F_1 score curves generally have an inverse- U shape and that the best static thresholds for all three cities are between 0.45-0.6. Such results indicate we need a high amount of evidence (i.e., probability estimates) to quantify any abnormal event so that the model tends to have a low false-positive rate.

Table 3 shows that our model in the best case yields a lower false-positive rate in Atlanta and Palo Alto than in Los Angeles; it can capture a very high number of actual ramping events in all three places as well. In particular, the performance of the dynamic threshold measured in F_1 score in Palo Alto (i.e., North California) is much higher than that of a static threshold. In the other two cities, the performance between static vs. dynamic thresholds is comparable.

Figure 10 shows that dynamic thresholds closely follow the pattern in our point predictions and our point predictions (red/blue dots) highly correlate with the actual ramping events (black dots). Together with Table 3 discussed earlier, it is thus clear that unless the predicted ramping probabilities are separated from the predicted normal probability (e.g., in Downtown Atlanta), prediction accuracy is higher using a dynamic threshold. When these two sets of probabilities intersect each other a lot (e.g., in Palo Alto), only predictions under dynamic thresholds perform satisfactorily. Also, we use the bootstrap confidence interval for β , which was shown in Figure 6, to compute the confidence interval for p_{tk} . We can see that the confidence intervals at 95% confidence level are not wide, even if Bonferroni correction was used.

In general, we note that picking the best static threshold is quite hard when data are highly non-stationary, so that in the long run, it may not be practical to stick to one single threshold for prediction. Furthermore, different sensor locations will lead to different best static threshold values, so it is also computationally efficient to quickly generate static thresholds for multiple locations. Thus, we can conclude that unless our abnormal and ramping predicted probabilities can be separated, using a dynamic threshold is more efficient and accurate, helping us reduce non-stationarity.

³Definitions: precision = $\frac{\# \text{True Positive}}{\# \text{Predicted Ramping Events}}$, recall = $\frac{\# \text{True Positive}}{\# \text{Ramping Events in Data}}$, $F_1 = \frac{2 \text{precision} \cdot \text{recall}}{\text{precision} + \text{recall}}$

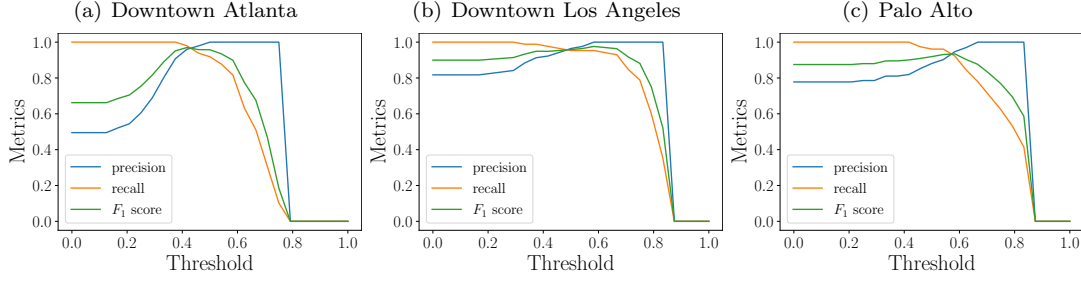


Figure 9: Accuracy metrics vs. static threshold at different locations. Static thresholds that lead to the highest F_1 scores on the first 30% of data are used during prediction.

Table 3: Sequential prediction performance for single-state model: precision, recall, and F_1 score in three downtown under static vs. dynamic threshold after tuning. The highest value among the four methods (LS or MLE combined with static or dynamic threshold) is in bold.

Location	τ	Least Square			Maximum Likelihood		
		Precision	Recall	F_1	Precision	Recall	F_1
Atlanta	Static	0.79	0.95	0.86	0.97	0.98	0.97
	Dynamic	0.82	0.95	0.88	0.96	0.96	0.96
Los Angeles	Static	0.91	0.78	0.84	0.91	0.81	0.86
	Dynamic	0.91	0.83	0.87	0.85	0.91	0.88
Palo Alto	Static	0.95	0.60	0.73	0.94	0.52	0.67
	Dynamic	0.78	0.89	0.83	0.76	0.88	0.82

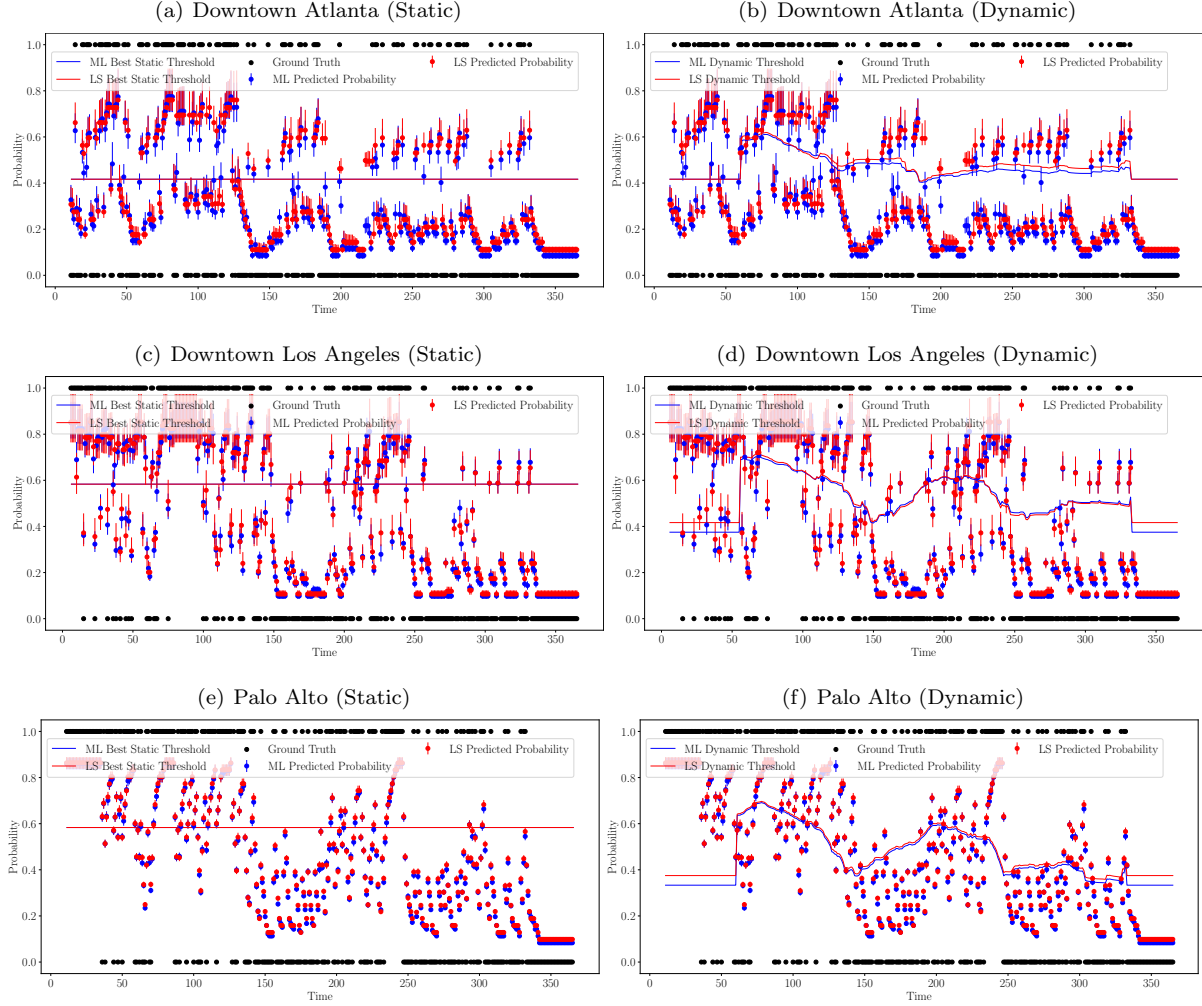


Figure 10: Confidence intervals for online point prediction of probabilities for single-state ramping events using LS (red dots) and ML (blue dots), compared with true ramping events (black dots). Left column is generated using static threshold and right column uses dynamic threshold. Dynamic thresholds separate the set of predicted ramping vs. normal probabilities better than static thresholds do.

4.3 Multi-state anomaly event

We perform a similar set of experiments as we did in the single-state section. Figures appear in the appendix and we summarize our findings below. First, we separately visualize these recovered parameters on map, as in Figure 12 (Positive-to-Positive) and in Figure 13 (Negative-to-Negative). Then, we present tables that measure accuracies in the multi-state cases. Table 4 records results from positive cases ($m = 1$) and Table 5 records results from negative cases ($m = 2$). To help analyze these tables, we lastly plot the point predictions and static/dynamic thresholds with bootstrap confidence intervals in Figure 14. Note we define $\omega_{tk} \in \{0, 1, \dots, M\}$ in the modeling section but to make sure the plots look appropriate, $\omega_{tk} = 2$ is changed to -1 in the plots here.

4.3.1 Visualize these influences on terrain map

Similar as we did in the last section, we only discuss MLE results. In the following analyses, we first discuss influences from positive ramping events to positive ramping events, i.e., positive-to-positive influences. Then we discuss negative-to-negative influences. Estimates of negative-to-positive or positive-to-negative are

essentially zero, so they are omitted. Upon analyzing these recovered parameters on map, we can find the following temporal patterns:

Positive-to-positive influences:

- In Atlanta, only the lower-left sensor has strong birthrate. Regarding influence parameters, at $s = 1$, horizontal estimates are strong at all latitudes. At $s = 5$, some strong estimates at the beginning disappeared, but overall directions and relative magnitude stay the same. At $s = 10$, the pattern persists. Some influences from west to east disappear.
- In Los Angeles, sensors closer to downtown have stronger birthrates. Regarding influence parameters, at $s = 1$, influences flow toward the middle from all directions. At $s = 5$ and 10, interactions decay but exist almost everywhere, especially west of downtown.
- In Northern California, we observe high birthrates on the northwest and east sides of the valley, but other places have small birthrates. Regarding influence parameters, at $s = 1$, it influences flow towards the direction of silicon valley (i.e., north west). There are clear influences from places onto themselves. At $s = 5$ and 10, we see a similar pattern and direction of influence but the magnitude of influences decreases dramatically.

Negative-to-negative influences:

- In Atlanta, birthrates are stronger at the corners and downtown than in other places. Regarding influence parameters, at $s = 1$, latitude-wise influences are weaker than longitude-wise ones. We also see some flow from west to east. At $s = 5$ and 10, influences almost all disappear, even under magnification.
- In Los Angeles, birthrates have similar magnitudes, except the one on the southeast corner. Regarding influence parameters, at $s = 1$, influences exist more along latitudes than along longitude. At $s = 5$ and 10, we see fast decay in magnitude, even under strong magnification. Only influences south of downtown and northeast of downtown exist.
- In Northern California, birthrates are all similar in magnitude except at South San Jose. Regarding influence parameters, at $s = 1$, results are mostly similar to positive-to-positive ones, except for the strong influence from Sunnyvale to San Jose (reversed in positive-to-positive case). At $s = 5$, we can only see influence from Sunnyvale to Mountain View and Sunnyvale to South San Jose, besides some past influences from a certain location onto itself. Some of these also decrease a lot in magnitude. At $s = 10$, only Sunnyvale to Mountain View exists, besides influences at certain locations onto itself.

In retrospect, we observe interesting differences between positive-to-positive (PP) and negative-to-negative (NN) ones, especially the directions along which influences exist. Generally, PP influences persist longer than NN; we see this from the size of edge widths when $s > 1$. Spatially, in positive-to-positive recovery, we find that interactions among sensors in Atlanta can be sparser than those in Los Angeles; in single-state recovery, Atlanta interactions are, however, denser than Los Angeles results. Birthrates are comparable in these two places. On the other hand, interaction among sensors in Northern California also becomes weaker in positive-to-positive recovery than in the single-state recovery. The level of the sparsity of interactions in Northern California is similar to that in Los Angeles. Birthrate results in Northern California are still closer to those in Los Angeles. In negative-to-negative recovery, interactions at all locations are relatively weak after $s > 1$. However, birthrates at all these locations are more comparable to each other.

4.3.2 Prediction Performance

Table 4 and Table 5 show prediction accuracies for positive and negative two-state ramping event, from which we see the following patterns. Predictions using MLE under dynamic threshold lead to the highest F_1 scores among 3 out of 6 situations. Each situation denotes results at a city under different prediction methods for either positive or negative cases. We expect such behavior to happen because ML has better theoretical performance under a large sample size than LS, and the dynamic threshold is expected to outperform the

static threshold. In particular, we notice that the best prediction performance in terms of precision, recall, or F_1 score is better under multi-state modeling than under single-state modeling. This shows that our model can analyze the type of ramping events separately and perform better when doing so.

Figure 14 that shows the point predictions and static/dynamic thresholds for multi-state cases provides further insights into our model’s satisfactory behaviors. Similar to the single-state plots (Figure 10), we first notice that dynamic thresholds closely follow the pattern in our point predictions, and our point predictions (red/blue dots) highly correlate with the actual ramping events (black dots). Compared to the single-state Figure 10, we can see that the set of predicted ramping probabilities and the set of predicted normal probabilities intersect much less in the multi-state case and that the positive or negative cases often occur in sequence. Together with Table 4 and Table 5 discussed earlier, we again see that the model achieves high accuracy when these two sets of predicted probabilities intersect each other less heavily. We used the same bootstrap techniques to provide confidence intervals on predicted point probabilities. We can also see from the figures that the confidence intervals are very narrow. When the empirical standard errors are too small to be noticeable (e.g., California), the resulting confidence intervals may be barely noticeable.

4.4 Fitting different models in different seasons

We treat seasonality as an important factor affecting the performance of our model. As shown in Figure 11, we could see the winter rainfall level is almost 0 in San Francisco while it rains a lot in summer, so that we expect fitting separate models in different seasons to give us a better estimation for the anomaly events.⁴

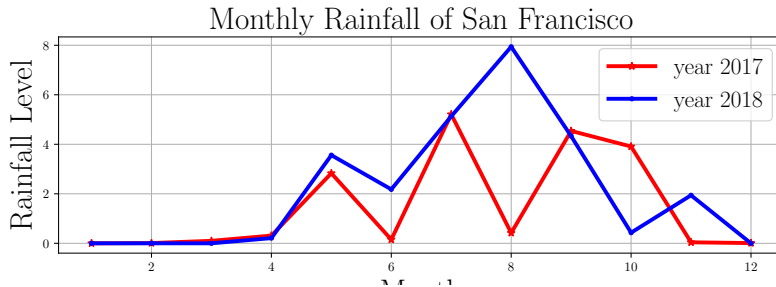


Figure 11: Monthly rainfall level of Year 2017 and 2018 in San Francisco. There are little rainfall from January to April but heavy rainfall from July to September.

Since there is a clear seasonal rainfall pattern in North California, we consider fitting different models on subsets of data with varying levels of rainfall. In particular, we fit both LS and ML models on January (01/01) till March (03/31) data and on July (07/01) till September (09/30) data in 2017, resulting in four separate models. The test data for each model are from the same range of months in 2018. Overall, we notice that fitting different models under these seasons can sometimes bring additional prediction performance gain. The spatial-temporal influence parameters do not have significant differences across seasons in single-state modeling; in multi-state modeling, influence parameters behave differently because of the big difference in the number of positive and negative abnormal events in each season.

We make almost the same plots as in earlier sections but compare estimation and prediction results from the two different seasons side by side. We show single-state results first before showing multi-state results. The complete set of figures are contained in Section B.2. We choose not to show bootstrap confidence/prediction intervals because we mainly want to compare the influence parameters and predictions results between results from these two seasons; adding confidence/prediction intervals makes the plots less clear.

4.4.1 Single-state results

First we show the recovered spatial-temporal influence as in Section 4.2.2. We can see that estimates from different seasons do not differ much. Next we visualize influence parameters on terrain map as in Section

⁴Rainfall data achieved from <https://ggweather.com/sf/monthly.html>

4.2.3. We only choose to show ML results here as we did earlier. We do not see much difference among the influences, despite some visible differences in terms of birthrate. We show the sequential prediction performance as in Table 3. We remark that the F_1 scores here in any season are better than earlier single-state results. Finally, we show the online point prediction of probabilities as in Figure 10. Note, because our dynamic threshold depends on the past abnormal value (yet there are very few here), the dynamic thresholds look almost like a flat line. We thus see few contributions from past abnormal events to the calculation of the current dynamic threshold.

4.4.2 Multi-state results

First we visualize influence parameters on terrain map as in Section 4.2.3. We only show ML results here. The first panel is positive-to-positive (PP) results, and the second is negative-to-negative (NN) results. Because of the big difference in the number of positive and negative ramp events in each season, the influence parameters look very different across seasons. In particular, under high rainfall (January-March), we see many more positive ramping events than negative ramping events, and the reverse situations occur under low rainfall (July-September). We suspect such situations occur because radiation is typically very low during the high rainfall season. Hence, a negative ramping event with a much lower radiation level than other events rarely occurs. The reverse reasoning applies to ramping events in the low rainfall season.

Next we show the sequential prediction performance as in Table 3. Note that PP and NN prediction performances are different for these two seasons. Some cells are 0 because there is no ramping event of a given type during that season. The model does not predict the positive ramping event for July till September 2018 and does not predict January’s negative ramping event till March 2018. Under single-state modeling, this situation does not happen because positive and negative ramping events are all considered equally as ramping events. The highest of these accuracy measures are higher than the earlier best multi-state results.

Finally, we show the online point prediction of probabilities in Figure 10, where the behavior is nearly identical to earlier results.

5 Conclusion and future works

This paper introduces a new framework for modeling spatial-temporal abnormal events in solar radiation, which can be divided into three steps: Anomaly extraction, model fitting, and anomaly prediction. We apply the method to various regions to show that the model is flexible and has different interpretations. We discuss the non-stationarity in solar radiation by comparing the difference between anomaly patterns in summer and winter in Section 4.4. We propose using the dynamic threshold in the prediction procedure to overcome this issue and lead to better accuracy. There are a few possible extensions: first, the empirical setting dynamic threshold can be improved by a theoretically guaranteed algorithm; second, there are other ways to extract ramping events, which could give us more types of abnormal events and lastly, we could go beyond binary or double-categorical prediction such that we can set different levels of abnormal events. In conclusion, this paper’s proposed model is a quite general framework and has many tunable parts mentioned above. Thus it can potentially be applied to any spatial-temporal events modeling task besides the solar radiation scenario.

Acknowledgements

The first three authors are supported by NSF CCF-1650913, NSF DMS-1938106, NSF DMS-1830210, and CMMI-2015787.

References

- [1] Mohamed Abuella and Badrul Chowdhury. Forecasting of solar power ramp events: A post-processing approach. *Renewable Energy*, 133:1380 – 1392, 2019.
- [2] Charu C Aggarwal. Outlier analysis. In *Data mining*, pages 237–263. Springer, 2015.

- [3] Leman Akoglu, Hanghang Tong, and Danai Koutra. Graph based anomaly detection and description: a survey. *Data mining and knowledge discovery*, 29(3):626–688, 2015.
- [4] Yang Cao, W. Wei, C. Wang, S. Mei, S. Huang, and X. Zhang. Probabilistic estimation of wind power ramp events: A data-driven optimization approach. *IEEE Access*, 7:23261–23269, 2019.
- [5] Ming-Dah Chou. A solar radiation model for use in climate studies. *Journal of the Atmospheric Sciences*, 49(9):762–772, 1992.
- [6] M. Cui, J. Zhang, A. R. Florita, B. Hodge, D. Ke, and Y. Sun. An optimized swinging door algorithm for wind power ramp event detection. In *2015 IEEE Power Energy Society General Meeting*, pages 1–5, 2015.
- [7] Mingjian Cui, Jie Zhang, Cong Feng, Anthony R. Florita, Yuanzhang Sun, and Bri Mathias Hodge. Characterizing and analyzing ramping events in wind power, solar power, load, and netload. *Renewable Energy*, 111, 4 2017.
- [8] Mingjian Cui, Jie Zhang, Anthony R Florita, Bri-Mathias Hodge, Deping Ke, and Yuanzhang Sun. An optimized swinging door algorithm for identifying wind ramping events. *IEEE Transactions on Sustainable Energy*, 7(1):150–162, 2015.
- [9] Jeff Dozier. A clear-sky spectral solar radiation model for snow-covered mountainous terrain. *Water Resources Research*, 16(4):709–718, 1980.
- [10] Nan Du, Hanjun Dai, Rakshit Trivedi, Utkarsh Upadhyay, Manuel Gomez-Rodriguez, and Le Song. Recurrent marked temporal point processes: Embedding event history to vector. In *Proceedings of the 22nd ACM SIGKDD International Conference on Knowledge Discovery and Data Mining*, pages 1555–1564, 2016.
- [11] A. Florita, B. Hodge, and K. Orwig. Identifying wind and solar ramping events. In *2013 IEEE Green Technologies Conference (GreenTech)*, pages 147–152, 2013.
- [12] Anthony Florita, Bri-Mathias Hodge, and Kirsten Orwig. Identifying wind and solar ramping events. In *2013 IEEE Green Technologies Conference (GreenTech)*, pages 147–152. IEEE, 2013.
- [13] Pinde Fu and Paul M Rich. A geometric solar radiation model with applications in agriculture and forestry. *Computers and electronics in agriculture*, 37(1-3):25–35, 2002.
- [14] Frank E Grubbs. Procedures for detecting outlying observations in samples. *Technometrics*, 11(1):1–21, 1969.
- [15] Manish Gupta, Jing Gao, Charu C Aggarwal, and Jiawei Han. Outlier detection for temporal data: A survey. *IEEE Transactions on Knowledge and data Engineering*, 26(9):2250–2267, 2013.
- [16] Alan G Hawkes. Spectra of some self-exciting and mutually exciting point processes. *Biometrika*, 58(1):83–90, 1971.
- [17] Simon Hawkins, Hongxing He, Graham Williams, and Rohan Baxter. Outlier detection using replicator neural networks. In *International Conference on Data Warehousing and Knowledge Discovery*, pages 170–180. Springer, 2002.
- [18] Valerie Isham and Mark Westcott. A self-correcting point process. *Stochastic processes and their applications*, 8(3):335–347, 1979.
- [19] Anatoli Juditsky, Arkadi Nemirovski, Liyan Xie, and Yao Xie. Convex recovery of marked spatio-temporal point processes. *arXiv preprint arXiv:2003.12935*, 2020.
- [20] Chandrika Kamath. Understanding wind ramp events through analysis of historical data. In *IEEE PES T&D 2010*, pages 1–6. IEEE, 2010.

- [21] Shuang Li, Shuai Xiao, Shixiang Zhu, Nan Du, Yao Xie, and Le Song. Learning temporal point processes via reinforcement learning. In *Advances in neural information processing systems*, pages 10781–10791, 2018.
- [22] M. Lukasik, Trevor Cohn, and Kalina Bontcheva. Point process modelling of rumour dynamics in social media. In *ACL*, 2015.
- [23] Hongyuan Mei and Jason M Eisner. The neural hawkes process: A neurally self-modulating multivariate point process. In *Advances in Neural Information Processing Systems*, pages 6754–6764, 2017.
- [24] T Muneer. Solar radiation model for europe. *Building services engineering research and technology*, 11(4):153–163, 1990.
- [25] Yu Nesterov. Semidefinite relaxation and nonconvex quadratic optimization. *Optimization Methods and Software*, 9(1-3):141–160, 1998.
- [26] Xi-Wei Tang and L. Li. Multivariate temporal point process regression. *arXiv: Methodology*, 2020.
- [27] LT Wong and WK Chow. Solar radiation model. *Applied energy*, 69(3):191–224, 2001.
- [28] Weichang Wu, Huanxi Liu, X. Zhang, Y. Liu, and H. Zha. Modeling event propagation via graph biased temporal point process. *IEEE transactions on neural networks and learning systems*, PP, 2020.
- [29] Shixiang Zhu, Ruyi Ding, Minghe Zhang, Pascal Van Hentenryck, and Yao Xie. Spatio-temporal point processes with attention for traffic congestion event modeling. *arXiv preprint arXiv:2005.08665*, 2020.
- [30] Shixiang Zhu, Minghe Zhang, Ruyi Ding, and Yao Xie. Deep attention spatio-temporal point processes. *arXiv preprint arXiv:2002.07281*, 2020.
- [31] W. Zhu, L. Zhang, M. Yang, and B. Wang. Solar power ramp event forewarning with limited historical observations. In *2019 IEEE/IAS 55th Industrial and Commercial Power Systems Technical Conference (I CPS)*, pages 1–8, 2019.

A MLE performance guarantee

We use notations in [19] to define a martingale-difference sequence $\{\xi_t\}_{t=1}^N$, so that $F_{\omega^N}(x) = \frac{1}{N} \sum_{t=1}^N \xi_t$. $F_{\omega^N}(x)$ will be abbreviated as $F(x)$ from now on.

Note that $F(x)$, the gradient of ML objective, was derived as

$$F_{\omega^N}(\beta) = \nabla L(\beta) = \frac{1}{N} \sum_{t=1}^N \eta(\omega_{t-d}^{t-1}) \theta(\eta^T(\omega_{t-d}^{t-1}) x, \omega_t),$$

with

$$\theta(z, \omega) = \nabla_z \mathcal{L}_\omega(z) = - \sum_{k=1}^K \left[\sum_{p=1}^M \frac{[w]_{kp}}{[z]_{kp}} e^{kp} - \frac{1 - \sum_{p=1}^M [w]_{kp}}{1 - \sum_{p=1}^M [z]_{kp}} \sum_{p=1}^M e^{kp} \right]$$

Thus, $\xi_t = \eta(\omega_{t-d}^{t-1}) \theta(\eta^T(\omega_{t-d}^{t-1}) \beta, \omega_t)$ with $\mathbb{E}[\xi_t] = 0$ and therefore, $\{\xi_t\}$ forms a martingale-difference sequence.

A.1 Proof of Lemma 3.2

Under notations above, we now provide a slightly more general version here:

Lemma A.1. *For all $\epsilon \in (0, 1)$ vector $F(\beta)$ satisfies*

$$\text{Prob}_{\omega^N} \left\{ \|F(\beta)\|_\infty \geq \Theta \sqrt{\frac{2 \ln(2\kappa/\epsilon)}{N}} \right\} \leq \epsilon, \rho \in (0, 1)$$

where Θ is a bound on $\|\xi_t\|_\infty$

Proof. We first provide a simple bound on $\|\xi_t\|_\infty$ and then link Θ to $\|\xi_t\|_\infty$ under MLE with identity-link. First,

$$\begin{aligned} \|\xi_t\|_\infty &= \|\eta(\omega_{t-d}^{t-1}) \theta(\eta^T(\omega_{t-d}^{t-1}) \beta, \omega_t)\|_\infty \\ &\stackrel{(i)}{\leq} \|\theta(\eta^T(\omega_{t-d}^{t-1}) \beta, \omega_t)\|_\infty \\ &\stackrel{(ii)}{=} \left\| \sum_{k=1}^K \left[\sum_{p=1}^M \frac{[w]_{kp}}{[z]_{kp}} e^{kp} - \frac{1 - \sum_{p=1}^M [w]_{kp}}{1 - \sum_{p=1}^M [z]_{kp}} \sum_{p=1}^M e^{kp} \right] \right\|_\infty \\ &\stackrel{(iii)}{\leq} \left\| \sum_{k=1}^K \sum_{p=1}^M \frac{[w]_{kp}}{[z]_{kp}} e^{kp} \right\|_\infty \\ &\stackrel{(iv)}{\leq} \left\| \sum_{k=1}^K \sum_{p=1}^M \frac{1}{\rho} e^{kp} \right\|_\infty \\ &\stackrel{(v)}{=} 1/\rho, \end{aligned}$$

where (i) holds because of the definition of η , (ii) holds because we let $z := \eta^T \beta, \omega := \omega_t$ for simpler notation, (iii) holds because we have $1 \geq \sum_{p=1}^M [w]_{kp}$ and $\sum_{p=1}^M [z]_{kp}$, (iv) holds because we have $0 \leq [w]_{kp} \leq 1$ and $[z]_{kp} \geq \rho$ by definition, and (v) holds because we see $\sum_{k=1}^K \sum_{p=1}^M e^{kp}$ is the vector of all 1's in \mathbf{R}^{KM} .

Also, denoting by $\mathbf{E}_{|\omega^t}$ the conditional expectation given ω^t and $i = 1, \dots, \kappa$, we have

$$\begin{aligned} \mathbf{E}_{\omega^{t+1}} \left\{ \exp \left\{ \sum_{s=1}^{t+1} \gamma [\xi_s]_i \right\} \right\} &= \mathbf{E}_{\omega^t} \left\{ \exp \left\{ \sum_{s=1}^t \gamma [\xi_s]_i \right\} \mathbf{E}_{\omega_{t+1}|\omega^t} \left\{ \exp \{ \gamma [\xi_{t+1}]_i \} \right\} \right\} \\ &\leq \mathbf{E}_{\omega^t} \left\{ \exp \left\{ \gamma \sum_{s=1}^t [\xi_s]_i \right\} \exp \{ \gamma^2 / 2\rho^2 \} \right\}, \end{aligned}$$

where the last inequality is due to the Hoeffding's inequality and, from the above bound that the conditional, ω^t given, distribution of $[\xi_{t+1}]_i$ is zero mean and is supported on $[-1/\rho, 1/\rho]$. By induction, we have

$$\mathbf{E}_{\omega^N} \left\{ \exp \left\{ \gamma \left[\sum_{t=1}^N \xi_t \right]_i \right\} \right\} \leq \exp \{ N \gamma^2 / 2 \rho^2 \}.$$

Now using Chernoff bound, we have

$$\begin{aligned} \text{Prob}_{\omega^N} \{ [F(\beta)]_i > \theta \} &= \text{Prob}_{\omega^N} \left\{ \frac{1}{N} \left[\sum_{t=1}^N \xi_t \right]_i > \theta \right\} \\ &\leq \exp \{ -\mu \theta \} \mathbf{E}_{\omega^N} \left\{ \exp \left\{ \mu \frac{1}{N} \left[\sum_{t=1}^N \xi_t \right]_i \right\} \right\} \\ &\leq \exp \left\{ -\mu \theta + \frac{\mu^2}{2\tilde{N}} \right\}, \end{aligned}$$

where $\tilde{N} = N\rho^2$. Now, if we let $\theta = \gamma/\sqrt{\tilde{N}}$ and $\mu = \tilde{N}\theta$, we simplify the above bound and use the union bound to get

$$\text{Prob}_{\omega^N} \left\{ \|F(\beta)\|_\infty > \gamma/\sqrt{\tilde{N}}\rho \right\} \leq 2\kappa \exp \{ -\gamma^2/2 \}, \quad \forall \gamma \geq 0$$

Finally, we let $\gamma = \sqrt{2\ln(2\kappa/\epsilon)}$ and $\Theta = 1/\rho$, where $1/\rho$ is the bound on $\|\xi_t\|_\infty$. Further simplification finishes the proof. \square

A.2 Proof of Theorem 3.3

We restate the theorem and provide its proof below:

Theorem A.2. *For every $p \in [1, \infty]$ and every ω^N one has*

$$\|\hat{\beta} - \beta\|_p \leq (1 - \rho)^2 \|F_{\omega^N}(\beta)\|_\infty / \sqrt{\theta_1(A)\theta_p(A)}.$$

As a result, given any $\rho \in (0, 1)$ and $\epsilon \in (0, 1)$, the probability of the event

$$\|\hat{\beta} - \beta\|_p \leq \frac{(1 - \rho)^2}{\rho} \sqrt{\frac{2\ln(2\kappa/\epsilon)}{N}} / \sqrt{\theta_1(A)\theta_p(A)} \quad (19)$$

is at least $1 - \epsilon$.

Proof. Since $F(x)$ is the gradient of the convex and continuously differentiable log-likelihood $L_{\omega^N}(x)$, $F(x)$ is continuous and monotone. Thus, the estimator $\hat{\beta}$ is a weak and strong solution to the variational inequality $VI[F, B_\rho]$ for B_ρ defined in (15). As a result, $\langle F(\beta) - F(\hat{\beta}), \beta - \hat{\beta} \rangle \geq 0$ and $F(\hat{\beta}) = 0$. In fact, under our ρ -strengthened constraint on β , we can prove that $\tilde{F}(\eta^T x)$, which is defined so that $\eta \tilde{F}(\eta^T x) = F(x)$ with $\eta \eta^T = \frac{1}{N} \sum_{t=1}^N \eta(\omega_{t-d}^{t-1}) \eta^T(\omega_{t-d}^{t-1})$, satisfies

$$\langle \tilde{F}(\eta^T \beta) - \tilde{F}(\eta^T \hat{\beta}), \eta^T(\beta - \hat{\beta}) \rangle \geq (1 - \rho)^{-2} \|\eta^T(\hat{\beta} - \beta)\|_2^2.$$

Now, by the earlier definition of $\theta_p(A) = \theta_p(\eta \eta^T)$, we can see that $\|\eta^T(\hat{\beta} - \beta)\|_2^2 = (\hat{\beta}^T - \beta^T) A (\hat{\beta} - \beta) \geq$

$\sqrt{\theta_1(A)\theta_p(A)}\|\hat{\beta} - \beta\|_1\|\hat{\beta} - \beta\|_p$. As a result,

$$\begin{aligned}
\|F(\beta)\|_\infty\|\hat{\beta} - \beta\|_1 &\geq \left\langle F(\beta) - F(\hat{\beta}), \beta - \hat{\beta} \right\rangle \\
&= \left\langle \tilde{F}(\eta^T \beta) - \tilde{F}(\eta^T \hat{\beta}), \eta^T (\beta - \hat{\beta}) \right\rangle \\
&\geq (1 - \rho)^{-2} \|\eta^T (\hat{\beta} - \beta)\|_2^2 \\
&\geq \sqrt{\theta_1(A)\theta_p(A)}\|\hat{\beta} - \beta\|_1\|\hat{\beta} - \beta\|_p
\end{aligned}$$

□

B Additional experimental

B.1 Multi-state anomaly event

Visualize MLE influences on terrain map

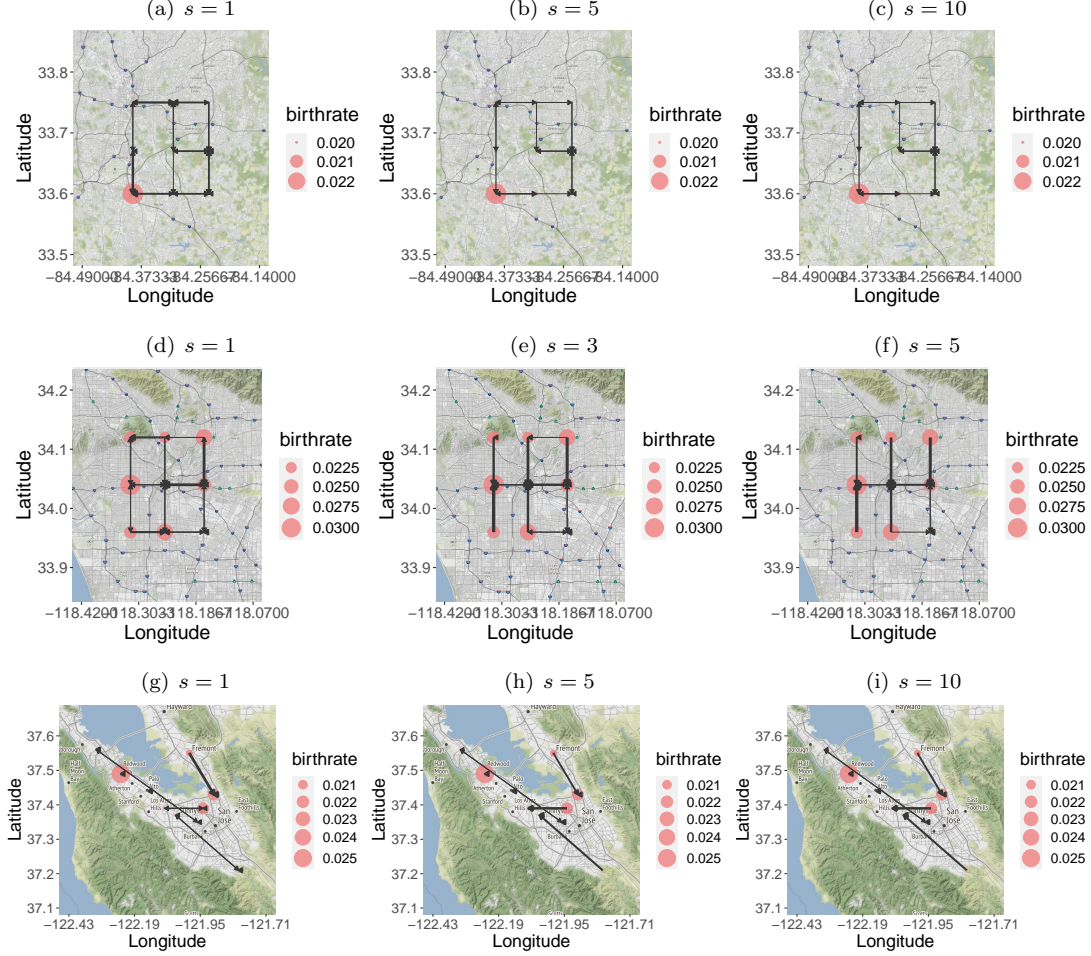


Figure 12: Multi-state positive-to-positive ($p = q = 1$) recovery results. To make sure the edges are visible when $s > 1$, we magnify edge weight of Atlanta (a-c) and Los Angeles (d-f) estimates 3 times and Northern California (g-i) estimates 5 times.

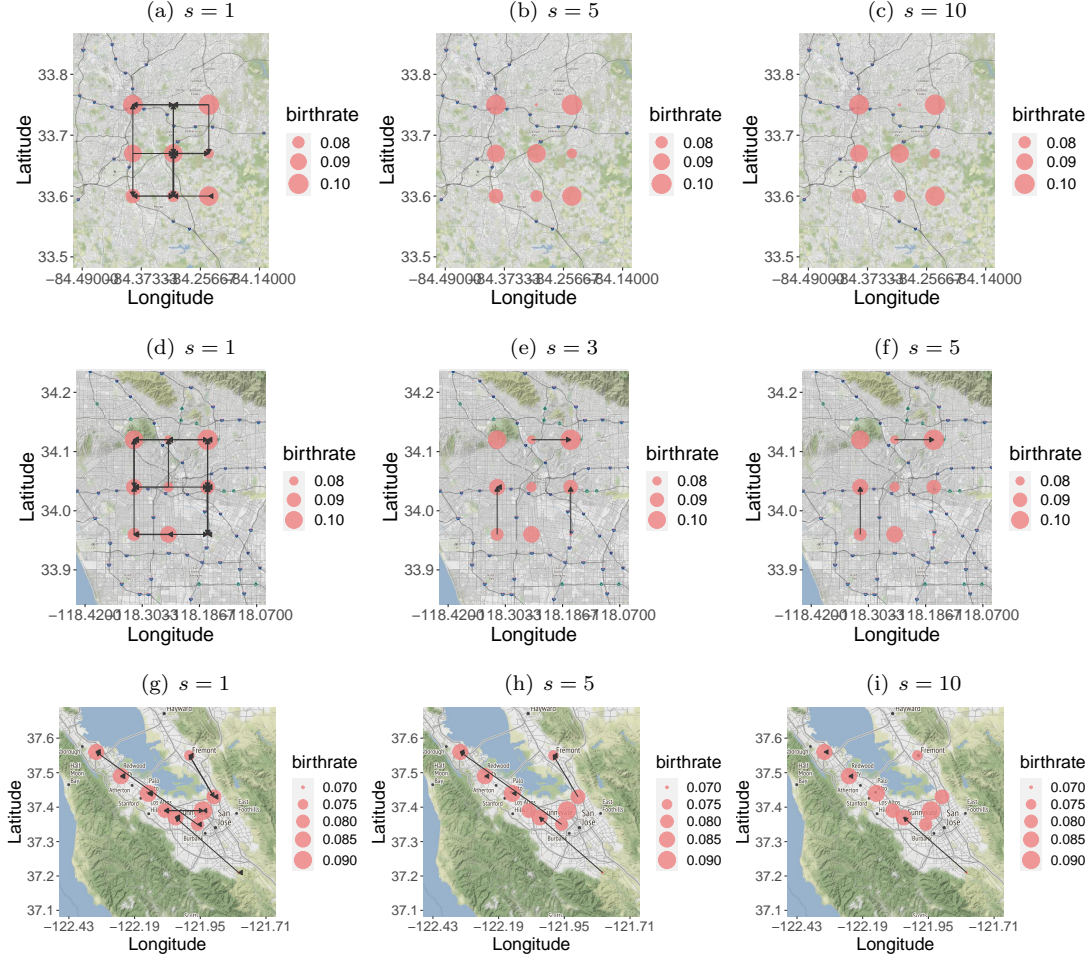


Figure 13: Multi-state negative-to-negative ($p = q = 2$) recovery result. To make sure the edges are visible when $s > 1$, we magnify edge weight of Atlanta (a-c) estimates 25 times, Northern California (g-i) estimates 5 times, and Los Angeles (d-f) estimates 6 times.

Prediction Performances

Table 4: Positive case for multi-state model: precision, precision, recall, and F_1 score in three downtown under static vs. dynamic threshold after tuning. The highest value among the four methods (LS or MLE combined with static or dynamic threshold) is in bold.

Location	τ	Precision	Least Square			Maximum Likelihood		
			Recall	F_1		Precision	Recall	F_1
Atlanta	Static	0.91	1.00	0.95		0.87	0.70	0.78
	Dynamic	0.91	1.00	0.95		0.87	0.70	0.78
Los Angeles	Static	1.00	0.79	0.88		0.96	0.79	0.86
	Dynamic	0.82	1.00	0.90		0.84	0.96	0.90
Palo Alto	Static	0.90	0.76	0.83		0.90	0.76	0.83
	Dynamic	0.81	1.00	0.89		0.93	1.00	0.96

Table 5: Negative case for multi-state model: precision, recall, and F_1 score in three downtown under static vs. dynamic threshold after tuning. The highest value among the four methods (LS or MLE combined with static or dynamic threshold) is in bold.

Location	τ	Precision	Least Square		Maximum Likelihood		
			Recall	F_1	Precision	Recall	F_1
Atlanta	Static	1.00	0.98	0.99	0.95	0.95	0.95
	Dynamic	0.95	0.98	0.96	0.91	0.95	0.93
Los Angeles	Static	0.18	1.00	0.31	0.80	0.87	0.84
	Dynamic	0.14	0.70	0.23	0.90	0.74	0.81
Palo Alto	Static	1.00	1.00	1.00	0.85	1.00	0.92
	Dynamic	0.86	1.00	0.93	1.00	0.98	0.99

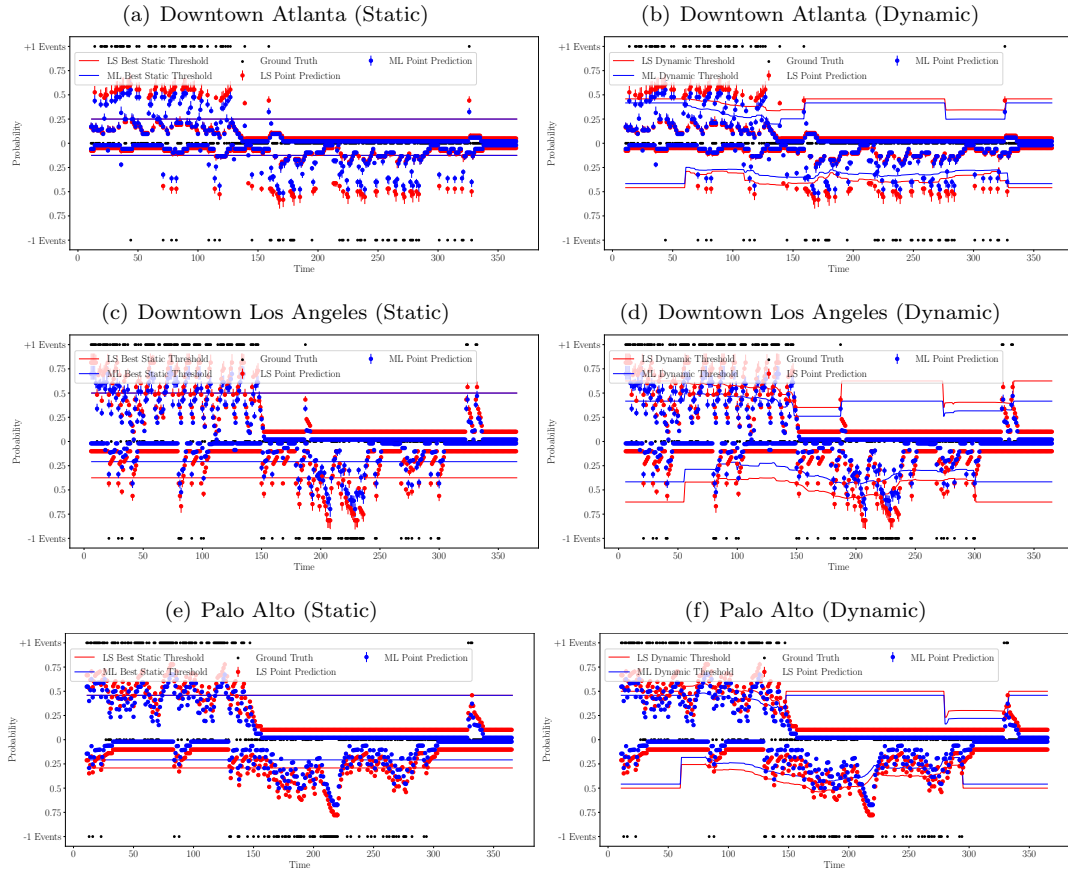


Figure 14: Confidence intervals for online point prediction of probabilities for multiple-state ramping events using LS (red dots) and ML (blue dots), compared with true ramping events (black dots). Left column is generated using static threshold and right column uses dynamic threshold.

B.2 Fitting Different models in different seasons

Single-state results

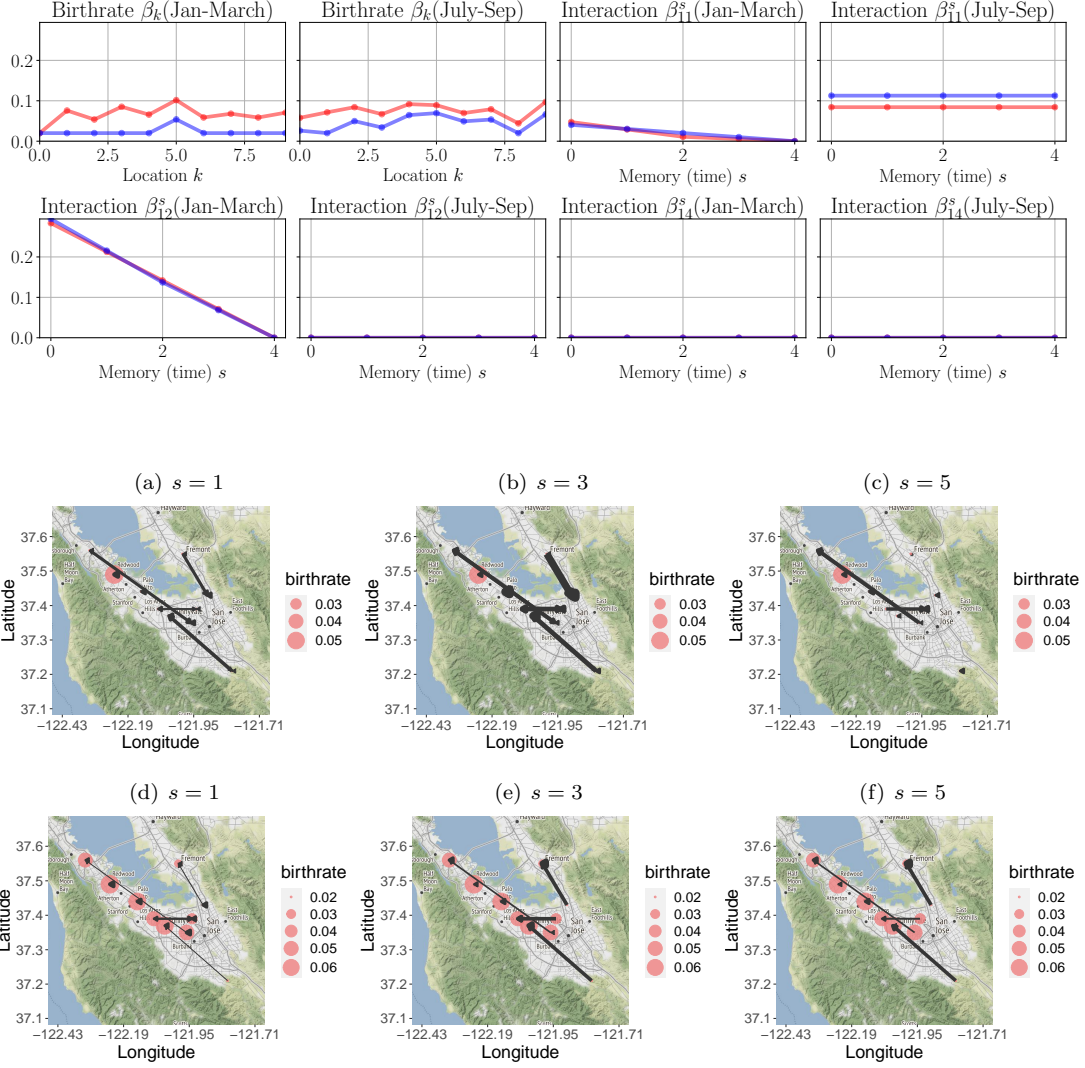


Figure 15: The first three figures show the learned visualization using data from first three months of 2017, the last three figures are learned from data from July to September in 2017.

Table 6: Sequential prediction performance for single-state model by rainfall levels: precision, recall, and F_1 score in Palo Alto under static vs. dynamic threshold after tuning. The higher value between static vs dynamic is in bold.

Months	τ	Precision	Least Square			Maximum Likelihood		
			Recall	F_1		Precision	Recall	F_1
Jan-Mar	Static	0.40	1.00	0.57		0.40	1.00	0.57
	Dynamic	1.00	0.77	0.87		0.91	0.81	0.86
July-Sept	Static	0.91	1.00	0.95		0.91	1.00	0.95
	Dynamic	1.00	0.90	0.95		1.00	0.85	0.92

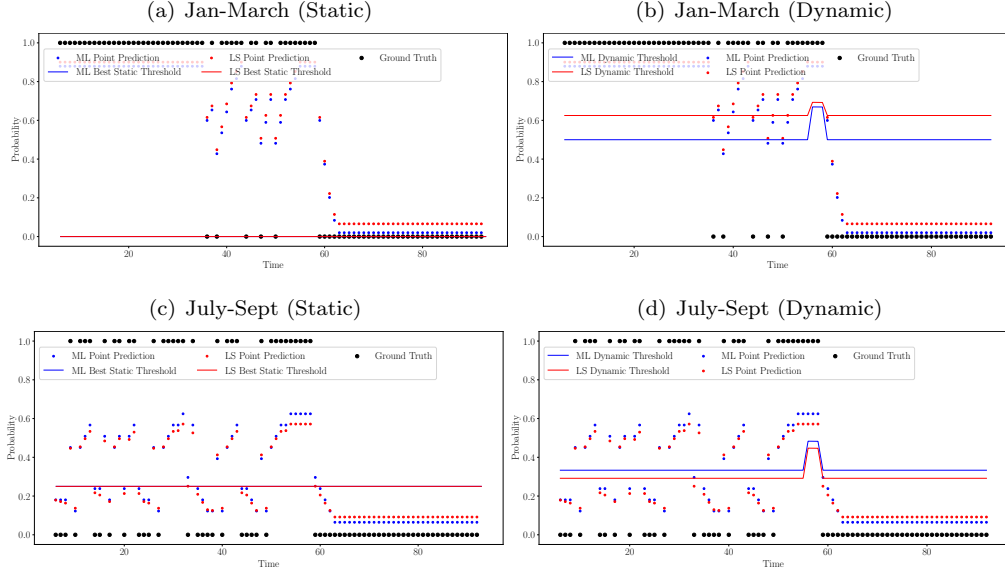


Figure 16: Online point prediction of probabilities for single-state ramping events using LS (red dots) and ML (blue dots), compared with true ramping events (black dots). Left column in each row is generated using static threshold and right column in each row uses dynamic threshold.

Multi-state results

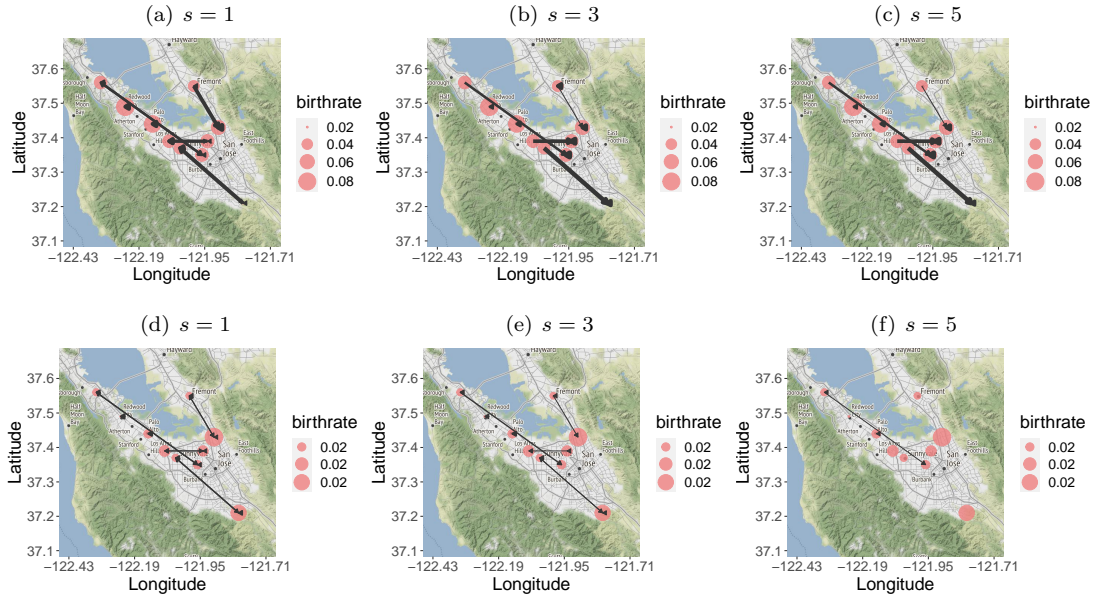


Figure 17: The first three figures show the learned visualization using data from first three months of 2017, the last three figures are learned from data from July to September in 2017.(PP) To make sure the edges are visible when $s > 1$, we magnify edge weight of Northern California (g-i) estimates 5 times.

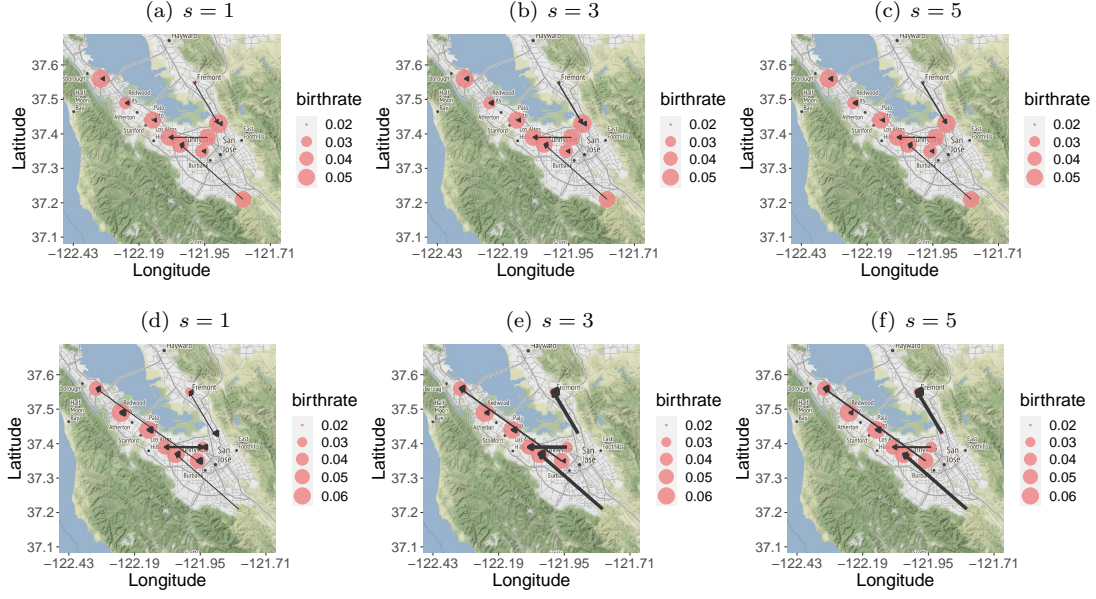


Figure 18: The first three figures show the learned visualization using data from first three months of 2017, the last three figures are learned from data from July to September in 2017.(NN) To make sure the edges are visible when $s > 1$, we magnify edge weight of Northern California (g-i) estimates 5 times.

Table 7: Multi-state sequential prediction performance for single-state model by rainfall levels: precision, recall, and F_1 score in Palo Alto under static vs. dynamic threshold after tuning. The higher value between static vs dynamic is in bold.

Months	τ	Precision	Least Square			Maximum Likelihood		
			Recall	F_1		Precision	Recall	F_1
PP: Jan-Mar	Static	1.00	1.00	1.00		1.00	1.00	1.00
	Dynamic	1.00	0.90	0.95		1.00	0.80	0.89
PP: July-Sept	Static	0.00	0.00	0.00		0.00	0.00	0.00
	Dynamic	0.00	0.00	0.00		0.00	0.00	0.00
NN: Jan-Mar	Static	0.00	0.00	0.00		0.00	0.00	0.00
	Dynamic	0.00	0.00	0.00		0.00	0.00	0.00
NN: July-Sept	Static	0.91	1.00	0.95		0.91	1.00	0.95
	Dynamic	1.00	0.90	0.95		1.00	0.85	0.92



Figure 19: Northern California: Online point predictions of probabilities for multi-state ramping events using LS (red dots) and ML (blue dots), compared with true ramping events (black dots). Left column in each row is generated using static threshold and right column in each row uses dynamic threshold.

B.3 Visualizing interactions via LS methods on terrain map

As we mentioned earlier, these parameters by LS are visually similar to those by ML.

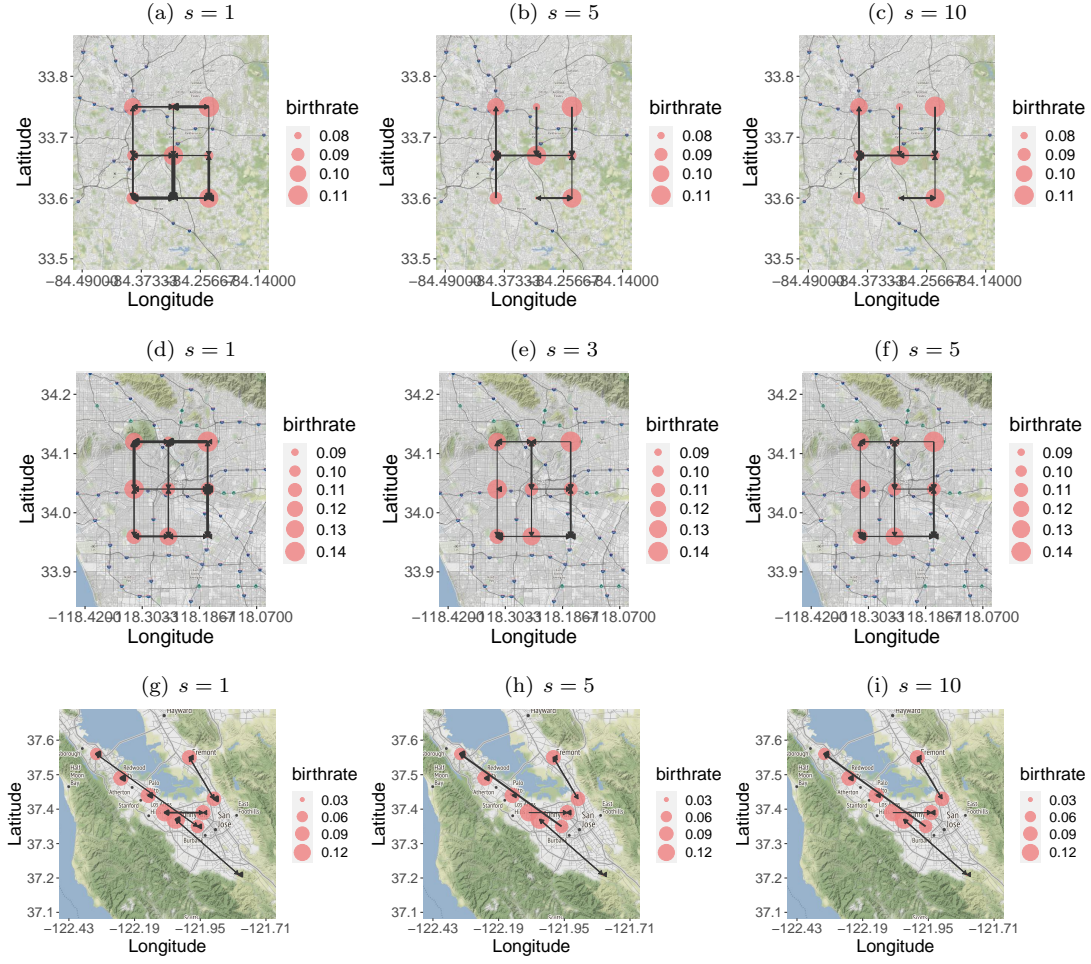


Figure 20: Map visualization for spatial-temporal interactions using LS method. To make sure the edges are visible when $s > 1$, we magnify edge weight of Atlanta (a-c) estimates 5 times, of Los Angeles (d-f) estimates 3 times, and of Northern California (g-i) estimates 5 times.

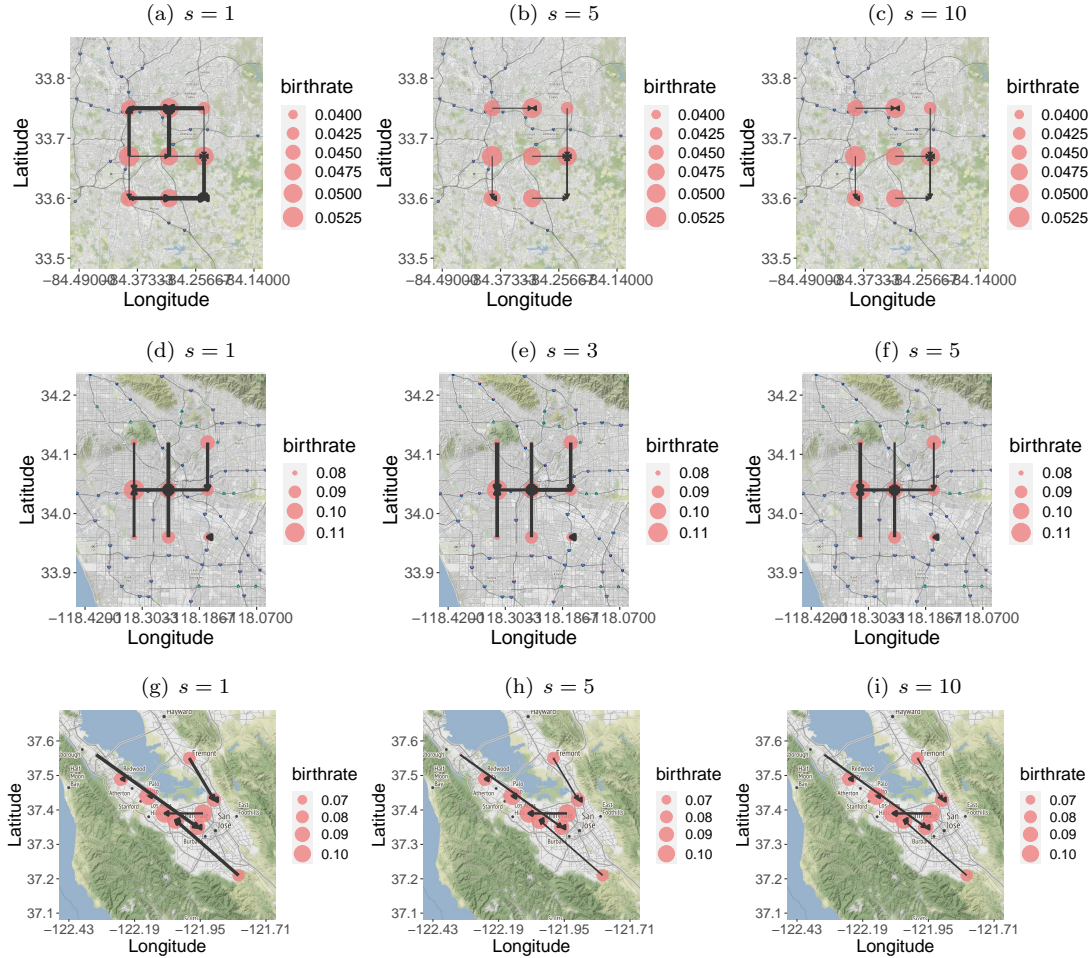


Figure 21: Map visualization for spatial-temporal interactions using LS method. Multi-state positive-to-positive ($p = q = 1$) recovery results. To make sure the edges are visible when $s > 1$, we magnify edge weight of Atlanta (a-c) and Los Angeles (d-f) estimates 3 times and Northern California (g-i) estimates 5 times.

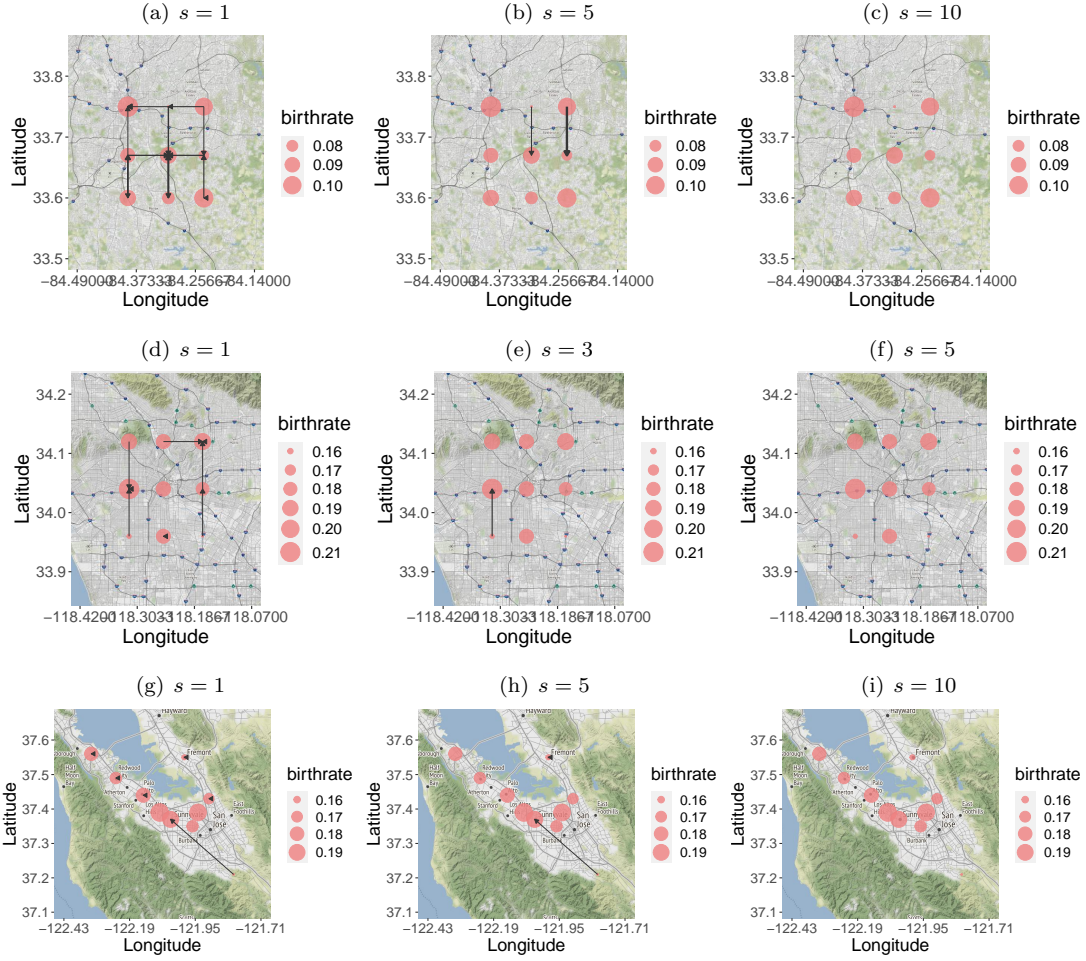


Figure 22: Map visualization for spatial-temporal interactions using LS method. Multi-state negative-to-negative ($p = q = 2$) recovery result. To make sure the edges are visible when $s > 1$, we magnify edge weight of Atlanta (a-c) estimates 25 times, Northern California (g-i) estimates 5 times, and Los Angeles (d-f) estimates 6 times.